LETTER

Population imaging of neural activity in awake behaving mice

Kiryl D. Piatkevich[1,2,11], Seth Bensussen[3,11], Hua-an Tseng[3,11], Sanaya N. Shroff[3], Violeta Gisselle Lopez-Huerta[4], Demian Park[1,2], Erica E. Jung[1,5], Or A. Shemesh[1,2], Christoph Straub[6], Howard J. Gritton[3], Michael F. Romano[3], Emma Costa[1], Bernardo L. Sabatini[6], Zhanyan Fu[4], Edward S. Boyden[1,2,7,8,9,10]* & Xue Han[3]*

A longstanding goal in neuroscience has been to image membrane voltage across a population of individual neurons in an awake, behaving mammal. Here we describe a genetically encoded fluorescent voltage indicator, SomArchon, which exhibits millisecond response times and is compatible with optogenetic control, and which increases the sensitivity, signal-to-noise ratio, and number of neurons observable several-fold over previously published fully genetically encoded reagents[1–8]. Under conventional one-photon microscopy, SomArchon enables the routine population analysis of around 13 neurons at once, in multiple brain regions (cortex, hippocampus, and striatum) of head-fixed, awake, behaving mice. Using SomArchon, we detected both positive and negative responses of striatal neurons during movement, as previously reported by electrophysiology but not easily detected using modern calcium imaging techniques[9–11], highlighting the power of voltage imaging to reveal bidirectional modulation. We also examined how spikes relate to the subthreshold theta oscillations of individual hippocampal neurons, with SomArchon showing that the spikes of individual neurons are more phase-locked to their own subthreshold theta oscillations than to local field potential theta oscillations. Thus, SomArchon reports both spikes and subthreshold voltage dynamics in awake, behaving mice.

Near-infrared genetically encoded voltage indicators (GEVIs) derived from rhodopsins offer high temporal fidelity, and are compatible with optogenetics[1,12,13], whereas green fluorescent GEVIs derived from the voltage-sensing domains of phosphatases or opsins are often slower and brighter[2,3,14–17]. Translating these voltage sensors into the living mammalian brain has been challenging, because of poor membrane localization, low photostability, and low signal-to-noise ratio (SNR). So far, amongst fully genetically encoded reagents, only Ace2N and paQuasAr3-s have been used to optically report voltage dynamics in a living mouse brain, reporting the activities of up to four cells in one field of view (FOV) in awake mice[4,17]. Recently, we developed a robotic directed-evolution approach and created the improved GEVI Archon1[13]. To further improve SNR in the dense, living mammalian brain, we conducted a screen for peptides to localize Archon1 to the soma[18–21], so that neuropil contamination could be reduced (Extended Data Fig. 1; see Supplementary Table 1 for the sequences of the motifs). The molecule Archon1–KGC–EGFP–K_V2.1-motif–ER2, which we call SomArchon (Fig. 1a), exhibited the highest relative change in fluorescence ($\Delta F/F$) during 100-mV voltage steps (Fig. 1g) and was well-localized to the soma (Extended Data Fig. 1h–k).

SomArchon fluorescently reported action potentials in mouse brain slices after in utero electroporation (IUE) into the cortex and hippocampus, and after adeno-associated virus (AAV)-mediated expression in the cortex, striatum, and thalamus (Extended Data Fig. 2). SomArchon was localized primarily to the membrane within 30–45 μm

of the cell body in the cortex, striatum, and hippocampus (Fig. 1b, Extended Data Fig. 1h–k). The sensitivity of SomArchon was about twofold greater (Fig. 1c, d) than our previously published values for Archon1[13], and it had comparable kinetics (Fig. 1e) and SNR (defined as the maximum fluorescence change observed during an action potential divided by the standard deviation of the baseline) (Fig. 1f). SomArchon linearly reported voltage (Fig. 1g), and did not alter membrane properties or resting potential in mouse brain slices, induce gliosis, or mediate light-induced phototoxicity (Extended Data Figs. 3, 4). It has previously been demonstrated that Archon1 exhibits essentially no crosstalk under blue light illumination as used commonly for optogenetic neural activation[13]. We used a bicistronic expression system (Fig. 1h) to co-express SomArchon and the high-performance channelrhodopsin CoChR[22] in the same cell, and demonstrated that brief blue light pulses could reliably evoke action potentials that were visible in SomArchon fluorescence (Fig. 1i, j).

We performed a side-by-side comparison of SomArchon with soma-localized versions of several next-generation voltage sensors—specifically QuasAr3-s[4], paQuasAr3-s[4], ASAP3[5], and Voltron$_{525}$[6]—in mouse cortical brain slices under identical expression conditions, focusing on layer 2/3 neurons (Supplementary Table 3). The spectrally similar sensors QuasAr3-s, paQuasAr3-s, and SomArchon were recorded under identical imaging conditions (1.5 W mm^{-2}) during CoChR-mediated action potentials. ASAP3 and Voltron were recorded with the filter sets described[5,6] under similar excitation intensities as used in the initial description of Voltron[6] (25–29 mW mm^{-2}), during action potentials evoked upon application of 4-aminopyridine. Under these conditions, SomArchon exhibited the highest $\Delta F/F$ and SNR per action potential (Extended Data Fig. 5); in addition, SomArchon exhibited values higher than those previously reported for Ace2N-mNeon[7], ASAP1[2], MacQ-mCitrine[3], and QuasAr2[8] (Supplementary Table 3). In addition, SomArchon showed higher photostability than soma-localized versions of ASAP3 and Voltron$_{525}$ under comparable imaging conditions in cultured neurons (Extended Data Fig. 5e).

We virally expressed SomArchon in vivo in the mouse motor cortex, visual cortex, striatum, and hippocampus, and imaged neural activity while mice were awake with their heads fixed under a conventional one-photon microscope (Fig. 2a) using a scientific complementary metal-oxide semiconductor (sCMOS) camera and laser excitation light at 637 nm, at a power of around 1.6 W mm^{-2} (75 mW; 20× objective lens), 4 W mm^{-2} (75 mW; 40× objective lens), or 1.6 W mm^{-2} (95 mW; 16× objective lens). Cells expressing SomArchon could be resolved at depths of about 50–150 μm below the imaging surface (Fig. 2b). We could detect individual spikes in single cells in all four brain regions (Fig. 2c, e, g, i, Supplementary Video 1). The SNR per action potential ranged from about 7 to about 16 across the brain regions examined (Fig. 2d, f, h, j). To our knowledge, no other paper has reported SNR

[1]Media Lab, MIT, Cambridge, MA, USA. [2]MIT McGovern Institute for Brain Research, MIT, Cambridge, MA, USA. [3]Department of Biomedical Engineering, Boston University, Boston, MA, USA. [4]Stanley Center for Psychiatric Research, Broad Institute of MIT and Harvard, Cambridge, MA, USA. [5]Department of Mechanical and Industrial Engineering, University of Illinois, Chicago, IL, USA. [6]Howard Hughes Medical Institute, Department of Neurobiology, Harvard Medical School, Boston, MA, USA. [7]Department of Biological Engineering, MIT, Cambridge, MA, USA. [8]MIT Center for Neurobiological Engineering, MIT, Cambridge, MA, USA. [9]Department of Brain and Cognitive Sciences, MIT, Cambridge, MA, USA. [10]Koch Institute, MIT, Cambridge, MA, USA. [11]These authors contributed equally: Kiryl D. Piatkevich, Seth Bensussen, Hua-an Tseng. *e-mail: esb@media.mit.edu; xuehan@bu.edu
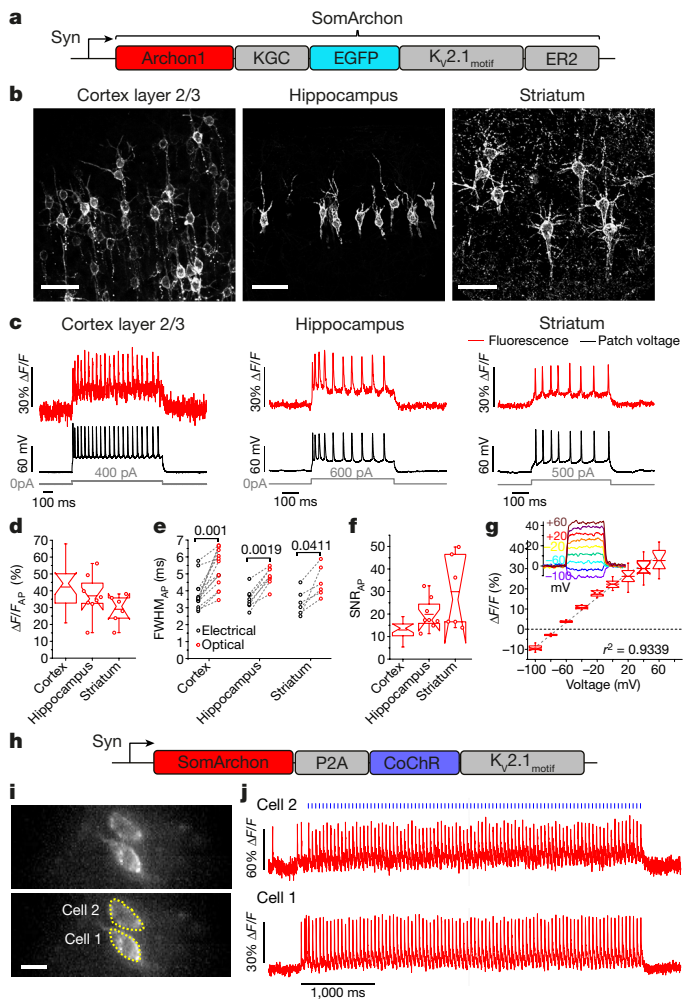
Fig. 1 | SomArchon enables high-fidelity voltage imaging in brain slices. a, Diagram of the SomArchon construct. **b**, Confocal images of SomArchon-expressing neurons in cortex layer 2/3 (left), hippocampus (middle), and striatum (right). Excitation wavelength (λ_{ex}) = 488 nm laser, emission wavelength (λ_{em}) = 525/50 nm (representative images selected from 8, 10 and 6 slices, respectively, from 2 mice each). Scale bars, 50 μm. **c**, Single-trial SomArchon fluorescence (red), and concurrent membrane voltage recorded via whole-cell patch-clamp (black), during action potentials evoked by current injection (grey); λ_{ex} = 637 nm laser at 0.8, 1.5, and 1.5 W mm^{-2} for cortex, hippocampus, and striatum, respectively. **d**, $\Delta F/F$ per action potential across recordings exemplified in **c** (representative traces selected from n = 18, 8, and 6 neurons from 5, 2, and 2 mice, respectively). Box plots: 25th and 75th percentiles with notch, median; whiskers, 1.5× interquartile range from the 25th and 75th percentiles; middle horizontal line, mean; individual data points, open circles when $n < 9$). **e**, Electrical and optical action potential waveform full-width-at-half-maximum (FWHM$_{AP}$; dashed lines connect the same neurons) across recordings exemplified in **c** (P values above brackets are from two-sided Wilcoxon rank-sum test; Supplementary Table 2). **f**, SNR per action potential across recordings exemplified in **c**. **g**, Population fluorescence of SomArchon in response to voltage steps in voltage-clamp mode, normalized to the fluorescence at −70 mV (inset, optical recordings for a representative neuron) recorded in cortex (n = 12 neurons from 2 mice). **h**, Diagram of SomArchon–P2A–CoChR–K$_V$2.1$_{motif}$. **i**, Fluorescence image of neurons in hippocampal slice expressing SomArchon–P2A–CoChR–K$_V$2.1$_{motif}$ (top) with two cells identified (bottom); λ_{ex} = 637 nm, exposure time 1.3 ms (selected from n = 3 slices from 2 mice). Scale bar, 25 μm. **j**, Representative single-trial optical voltage traces from cells shown in **i** with blue light stimulation (2 ms pulse at 20 Hz). Acquisition rate, 777 Hz.

values per action potential in living mouse brain, so we cannot directly compare our molecule to others in this regard. We were able to resolve short segments of proximal dendrites next to the soma, and detected

voltage fluctuation patterns that sometimes differed from those in the soma (Extended Data Fig. 6c–f). In addition, simultaneous optical control and voltage imaging was feasible using the strategy shown in Fig. 1h, in awake behaving mice (Fig. 2k–m).

Electrophysiological studies have shown that many striatal neurons increase their responses during movement[9,23], while others decrease their responses[9,10]. Although electrophysiological recordings largely discard spatial information regarding the relative locations of the neurons being observed, recent calcium imaging studies have revealed that spatially clustered striatal neurons are activated by similar aspects of movement[11]. These calcium imaging studies focused on the increases in activity during movement; decreases in activity are harder to observe with calcium imaging. We performed voltage imaging while mice ran on a spherical treadmill (Fig. 3a), identified cell bodies and spikes from cells in the striatum (Fig. 3b–d), and aligned spiking activity to movement (Fig. 3d). Some neurons exhibited firing patterns known to occur in striatal fast spiking interneurons[24] or cholinergic interneurons[25] (Extended Data Fig. 7a–d). We found that 4 of the 14 neurons imaged were positively modulated by movement speed, and that 2 were negatively modulated by movement speed (Fig. 3e, f, Extended Data Fig. 7e, f; see Supplementary Table 2 for statistics). Furthermore, adjacent neurons did not respond to movement speed in identical ways. For example, in two recordings of three neurons each, one of the three neurons was positively modulated by movement speed whereas the other two were not (Fig. 3f, Extended Data Fig. 7a, c (cells 1, 2, 3 and cells 6, 7, 8), Supplementary Table 2). Thus, SomArchon can readily detect decreases in striatal neuron spiking during movement, and can help to disambiguate activity changes amongst spatially clustered striatal neurons.

We performed wide-field voltage imaging with SomArchon in hippocampal CA1 neurons in awake, head-fixed mice, while simultaneously recording local field potentials (LFPs). In vivo patch-clamp recordings have shown that the spikes of a CA1 neuron are more strongly phase-locked to its own intracellular theta frequency (4–10 Hz) oscillations than to the theta oscillations of the across-neuron averaged LFP[26,27]. We found that 6 of the 16 neurons had spikes phase-locked to both intracellular and LFP theta oscillations (Fig. 4a), and that 9 were phase-locked only to intracellular theta oscillations and not to LFP theta oscillations (Fig. 4b). As a population, neurons exhibited stronger phase-locking to intracellular theta oscillations than to LFP theta oscillations (Fig. 4c, d). SomArchon thus supports the analysis of subthreshold intracellular oscillations, although interpretation of these measurements must take into account background fluorescence, which—in densely labelled tissue—may result in crosstalk that affects correlations.

We evaluated the photostability of SomArchon in vivo, and found a slight decrease in fluorescence intensity in both the striatum and the hippocampus over time. However, the SNR remained largely stable in both brain regions (Extended Data Fig. 8). In the hippocampus, firing rates remained constant over time, and we were able to continuously image for up to 80 s with minimal changes in SNR (Extended Data Fig. 8i–m, Supplementary Video 1). This lack of toxicity is consistent with our results from cultured neurons (Extended Data Fig. 3).

Owing to the high performance and soma-targeted nature of SomArchon, we were able to routinely image multiple neurons at once in both cortical and subcortical brain regions (Figs. 2k, l, 3b, c, Extended Data Fig. 6a, b). In the hippocampus, using a 20× objective lens, we were able to record from 14 neurons at once, 8 of which were spiking (Fig. 4e, f). In addition, using a 16× objective lens, we routinely recorded from around 13 cells at once (n = 13.1 ± 3.5 (mean ± s.d.) neurons per FOV from 13 recording sessions in 2 awake mice). Of the 170 manually identified neurons, 107 (63%) spiked during the recording periods (duration: 13.5–27 s) (Extended Data Fig. 6g–j, Supplementary Table 4). The ability to record from multiple neurons simultaneously enabled us to examine the correlation and coherence of subthreshold activities between pairs of neurons, although background fluorescence crosstalk between nearby neurons will need to
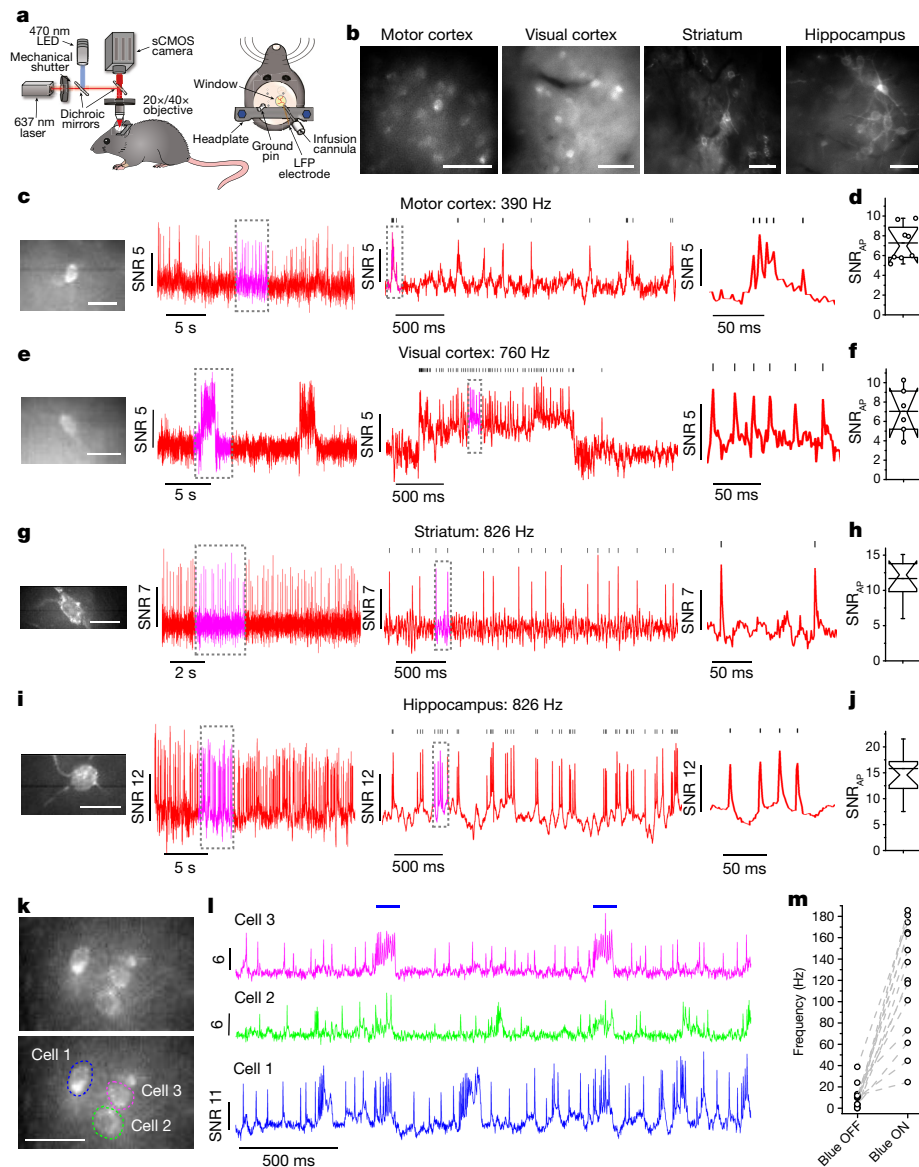

Fig. 2 | SomArchon enables single-cell voltage imaging in multiple brain regions of awake mice, using a simple wide-field imaging setup. **a**, Experimental setup. Left, awake mice had their heads fixed under a wide-field microscope; right, surgical window implant coupled with an infusion cannula and an LFP recording electrode. **b**, Representative SomArchon-expressing neurons visualized via EGFP fluorescence in motor cortex, visual cortex, striatum, and hippocampus ($\lambda_{ex} = 470/25$ nm LED, $\lambda_{em} = 525/50$ nm). Scale bars, 50 μm. **c**, **e**, **g**, **i**, Voltage imaging in motor cortex (**c**), visual cortex (**e**), striatum (**g**), and hippocampus (**i**). Left, SomArchon fluorescence image of the cell in vivo; right, optical voltage trace acquired from the cell (dashed boxes indicate time intervals shown at successively expanded time scales; vertical bars indicate peaks of action potentials identified by a custom spike-sorting algorithm). $\lambda_{ex} = 637$ nm laser at 1.6 W mm^{-2} for visual cortex and motor cortex, 4 W mm^{-2} for striatum and hippocampus, $\lambda_{em} = 664$ long-pass. Scale bars, 25 μm. **d**, **f**, **h**, **j**, Quantification of SNR per action potential for motor cortex (**d**), visual cortex (**f**), striatum (**h**), and hippocampus (**j**). Box plots as in Fig. 1. In **b**–**j**, representative images and traces were selected from, and statistics performed on, $n = 8, 6, 10$, and 17 cells from 3, 2, 3, and 4 mice for the motor cortex, visual cortex, striatum, and hippocampus, respectively. **k**, Fluorescence image of selected FOV showing hippocampal neurons expressing SomArchon–P2A–CoChR–K$_V$2.1$_{motif}$ (top) with neurons identified (bottom); $\lambda_{ex} = 637$ nm, exposure time 1.2 ms. Scale bar, 20 μm. **l**, Representative single-trial optical voltage traces from cells shown in **k** with blue light stimulation (100 ms pulse). Image acquisition rate, 826 Hz. **m**, Firing rate changes during blue light off versus blue light on conditions in individual neurons. In **k**–**m**, representative image selected from, and statistics performed on, $n = 14$ cells from 2 mice.

be considered when interpreting pairwise correlation and coherence measurements (Extended Data Figs. 9e–h, 10, Supplementary Discussion).

Compared to existing fully genetically encoded voltage indicators, SomArchon achieves a severalfold improvement in the number of cells that can be imaged simultaneously, while using inexpensive one-photon microscopy. The previously published record for fully genetically encoded voltage imaging was four spiking cells recorded simultaneously in an awake behaving mouse, but this required a specialized imaging setup that combined two-photon structural imaging to support patterned single-photon excitation illumination targeting individual cell bodies, as well as the blue-light-gated molecule paQuasAr3, which is incompatible with commonly used pulsed blue light optogenetic modulation[4]. ASAP3 has been used to image three dendrites at once, with 2-photon microscopy, but this approach can be used to record only single cells at the fast rates typical for voltage imaging[5]. The hybrid GEVI sensor Voltron enables imaging of 46 neurons[6], but requires the addition of chemicals delivered to the living brain that complicate in vivo mammalian use, is not compatible with optogenetics, and exhibits a lower dynamic range than SomArchon (Extended Data Fig. 5). Voltron, ASAP3, and Ace2N-mNeon all exhibit crosstalk with rhodopsins, hampering their use with optogenetic actuators. Voltage
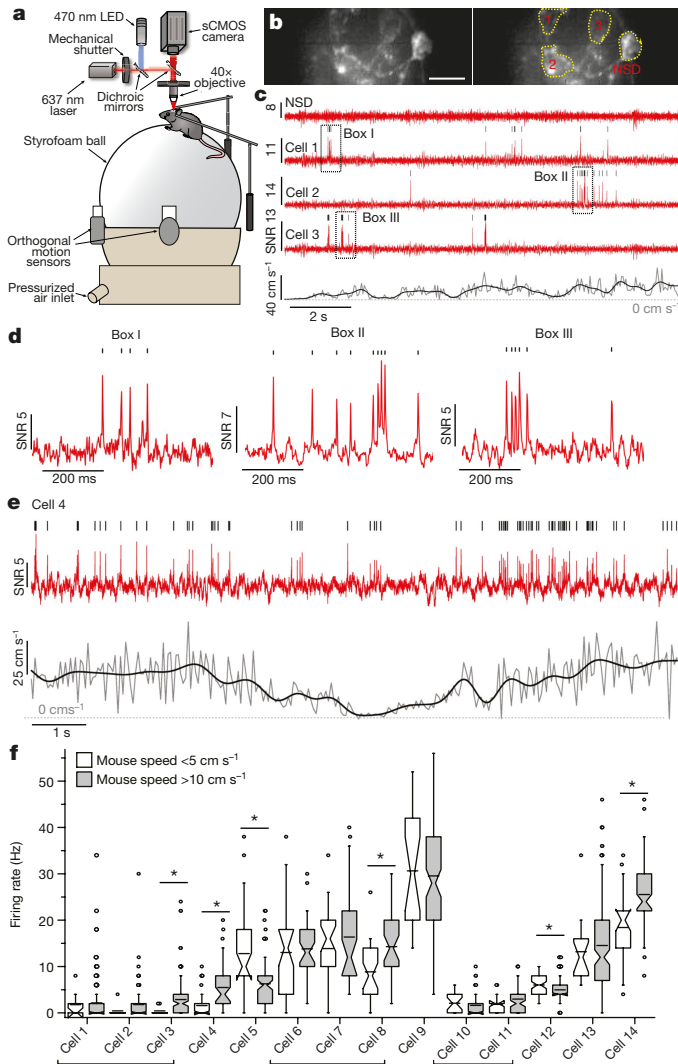
Fig. 3 | Voltage imaging of striatal neurons during locomotion. a, Schematic of the experimental setup, similar to that in Fig. 2a, but with mice positioned on a spherical treadmill. Imaging was performed with a $40\times$ objective lens. **b**, Left, SomArchon fluorescence image of striatal cells; right, identified regions of interest (ROIs) corresponding to somas. $\lambda_{ex} = 637$ nm, exposure time 1.2 ms (representative image selected from $n = 9$ FOV from 2 mice). Scale bar, 20 μm. NSD, no spikes detected. **c**, Optical voltage traces acquired from cells in **b** and corresponding mouse movement speed (black, low-pass-filtered at 1.5 Hz; grey, raw data; representative traces selected from $n = 2$ FOV from one mouse). Image acquisition rate, 826 Hz. **d**, Magnified views of the three periods indicated by black boxes in **c**. **e**, Optical voltage trace (red) for a neuron modulated by movement speed and corresponding movement speed (black and grey; representative trace selected from $n = 14$ neurons from 2 mice). **f**, Firing rates of individual striatal neurons, during periods with low (open box plots) versus high (grey box plots) movement speed ($n = 14$ neurons from 2 mice, brackets indicate neurons from the same FOV). *$P < 0.05$, two-sided Wilcoxon rank-sum test. Box plots as in Fig. 1.

imaging with SomArchon or QuasAr3 is limited mainly by the high power and illumination spot of the 637-nm excitation laser; however, our data suggest that high-powered 637-nm excitation does not induce more phototoxicity than is seen with common, lower-powered 470-nm excitation (Extended Data Fig. 3). In conclusion, SomArchon is fully genetically encoded, is compatible with conventional easily accessible one-photon wide-field fluorescence microscopes, is fully compatible with blue-light-driven optogenetics, and enables routine imaging of around 13 neurons in a single FOV. We anticipate that the practicality of SomArchon will enable its rapid deployment into a variety of contexts in neuroscience. As camera performance improves in years to
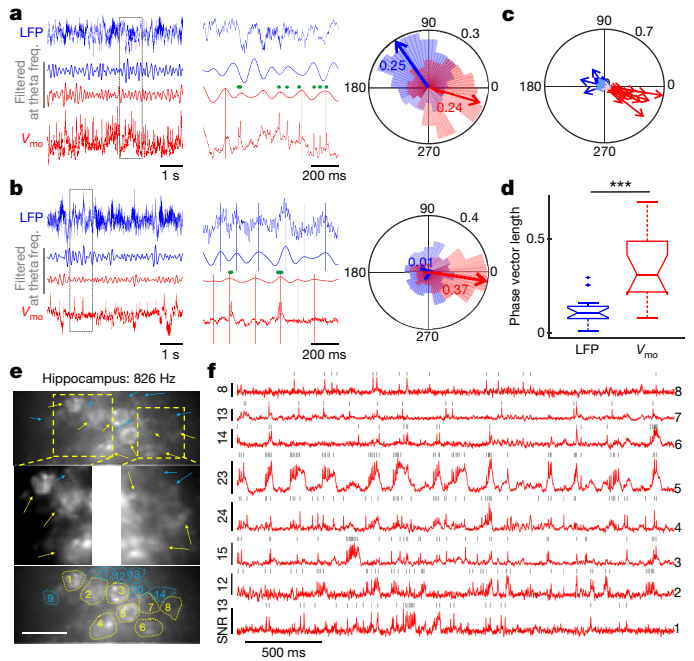

Fig. 4 | Population voltage imaging of spikes and subthreshold voltage activities in CA1 neurons. a, Neuron with spikes phase-locked to theta oscillations of LFPs (blue) and optically recorded membrane voltage (V_{mo}, red). Left, raw LFPs (top) and V_{mo} (bottom), and theta frequency-filtered traces (middle). Middle, magnified view of the boxed period on the left. Theta oscillation peaks are indicated by blue and red vertical lines, and spikes by green dots. Right, probability distribution of the timing of spikes relative to the phases of the LFP (blue) and V_{mo} (red) oscillations at theta frequency. Arrows indicate the average phase vector (with vector length indicated). Outer circle number indicates probability. Example selected from $n = 16$ neurons in 7 FOVs from 4 mice. **b**, As in **a**, but for an example neuron phase-locked to V_{mo} theta oscillations, but not to LFP theta oscillations. **c**, Population spike–phase vectors relative to theta oscillations of LFP (blue and light blue) and V_{mo} (red and pink). Each vector represents the average vector from one neuron (blue and red, $P < 0.05$; light blue and pink, not significant; χ^2 test, spike–phase distribution of each neuron against uniform distribution; $n = 198–1,077$ spikes per neuron; 16 neurons in 7 FOVs from 4 mice). **d**, Population spike–phase relationship. ***$P = 5.0 \times 10^{-5}$, two-tailed paired Student's t-test, $n = 16$ neurons in 7 FOVs from 4 mice. Box plots: 25th and 75th percentiles with notch, median; whiskers, all data points not considered outliers; plus, outliers. **e**, SomArchon fluorescence images of CA1 neurons (top) with ROIs overlaid (bottom; $n = 14$ FOV from 3 mice). Middle, zoomed-in views of the yellow boxes from the top. Yellow arrows, example spiking cells with optical voltage traces shown in **f**; blue arrows, neurons not active during the period shown. $\lambda_{ex} = 637$ nm laser at 1.5 W mm^{-2}. Scale bar, 20 μm.

come, and as further evolution of GEVIs continues, we anticipate that it might be possible to image tens to hundreds of neurons using simple one-photon optics in the near future.

Online content

Any methods, additional references, Nature Research reporting summaries, source data, extended data, supplementary information, acknowledgements, peer review information; details of author contributions and competing interests; and statements of data and code availability are available at https://doi.org/10.1038/s41586-019-1641-1.

1. Hochbaum, D. R. et al. All-optical electrophysiology in mammalian neurons using engineered microbial rhodopsins. *Nat. Methods* **11**, 825–833 (2014).
2. St-Pierre, F. et al. High-fidelity optical reporting of neuronal electrical activity with an ultrafast fluorescent voltage sensor. *Nat. Neurosci.* **17**, 884–889 (2014).

3. Gong, Y., Wagner, M. J., Zhong Li, J. & Schnitzer, M. J. Imaging neural spiking in brain tissue using FRET-opsin protein voltage sensors. *Nat. Commun.* **5**, 3674 (2014).
4. Adam, Y. et al. Voltage imaging and optogenetics reveal behaviour-dependent changes in hippocampal dynamics. *Nature* **569**, 413–417 (2019).
5. Chavarha, M. et al. Fast two-photon volumetric imaging of an improved voltage indicator reveals electrical activity in deeply located neurons in the awake brain. Preprint at https://www.biorxiv.org/content/10.1101/445064v2 (2018).
6. Abdelfattah, A. S. et al. Bright and photostable chemigenetic indicators for extended *in vivo* voltage imaging. *Science* **365**, 699–704 (2019).
7. Gong, Y. et al. High-speed recording of neural spikes in awake mice and flies with a fluorescent voltage sensor. *Science* **350**, 1361–1366 (2015).
8. Lou, S. et al. Genetically targeted all-optical electrophysiology with a transgenic Cre-dependent optopatch mouse. *J. Neurosci.* **36**, 11059–11073 (2016).
9. Jin, X., Tecuapetla, F. & Costa, R. M. Basal ganglia subcircuits distinctively encode the parsing and concatenation of action sequences. *Nat. Neurosci.* **17**, 423–430 (2014).
10. Shi, L. H., Luo, F., Woodward, D. J. & Chang, J. Y. Neural responses in multiple basal ganglia regions during spontaneous and treadmill locomotion tasks in rats. *Exp. Brain Res.* **157**, 303–314 (2004).
11. Gritton, H. J. et al. Unique contributions of parvalbumin and cholinergic interneurons in organizing striatal networks during movement. *Nat. Neurosci.* **22**, 586–597 (2019).
12. Flytzanis, N. C. et al. Archaerhodopsin variants with enhanced voltage-sensitive fluorescence in mammalian and *Caenorhabditis elegans* neurons. *Nat. Commun.* **5**, 4894 (2014).
13. Piatkevich, K. D. et al. A robotic multidimensional directed evolution approach applied to fluorescent voltage reporters. *Nat. Chem. Biol.* **14**, 352–360 (2018).
14. Jin, L. et al. Single action potentials and subthreshold electrical events imaged in neurons with a fluorescent protein voltage probe. *Neuron* **75**, 779–785 (2012).
15. Chamberland, S. et al. Fast two-photon imaging of subcellular voltage dynamics in neuronal tissue with genetically encoded indicators. *eLife* **6**, e25690 (2017).
16. Zou, P. et al. Bright and fast multicoloured voltage reporters via electrochromic FRET. *Nat. Commun.* **5**, 4625 (2014).
17. Gong, Y. et al. High-speed recording of neural spikes in awake mice and flies with a fluorescent voltage sensor. *Science* **350**, 1361–1366 (2015).
18. Shemesh, O. A. et al. Temporally precise single-cell-resolution optogenetics. *Nat. Neurosci.* **20**, 1796–1806 (2017).
19. Baker, C. A., Elyada, Y. M., Parra, A. & Bolton, M. M. L. Cellular resolution circuit mapping with temporal-focused excitation of soma-targeted channelrhodopsin. *eLife* **5**, e14193 (2016).
20. Daigle, T. L. et al. A suite of transgenic driver and reporter mouse lines with enhanced brain-cell-type targeting and functionality. *Cell* **174**, 465–480.e22 (2018).
21. Wu, C., Ivanova, E., Zhang, Y. & Pan, Z. H. rAAV-mediated subcellular targeting of optogenetic tools in retinal ganglion cells *in vivo*. *PLoS ONE* **8**, e66332 (2013).
22. Klapoetke, N. C. et al. Independent optical excitation of distinct neural populations. *Nat. Methods* **11**, 338–346 (2014).
23. Kravitz, A. V. & Kreitzer, A. C. Striatal mechanisms underlying movement, reinforcement, and punishment. *Physiology (Bethesda)* **27**, 167–177 (2012).
24. Koós, T. & Tepper, J. M. Inhibitory control of neostriatal projection neurons by GABAergic interneurons. *Nat. Neurosci.* **2**, 467–472 (1999).
25. Zhou, F. M., Wilson, C. J. & Dani, J. A. Cholinergic interneuron characteristics and nicotinic properties in the striatum. *J. Neurobiol.* **53**, 590–605 (2002).
26. Bittner, K. C. et al. Conjunctive input processing drives feature selectivity in hippocampal CA1 neurons. *Nat. Neurosci.* **18**, 1133–1142 (2015).
27. Harvey, C. D., Collman, F., Dombeck, D. A. & Tank, D. W. Intracellular dynamics of hippocampal place cells during virtual navigation. *Nature* **461**, 941–946 (2009).

METHODS

Molecular cloning. To screen candidates for the soma-localized Archon1 voltage sensor in primary hippocampal neurons, we synthesized DNAs coding for candidate localization motifs de novo with mammalian codon optimization and subcloned them with the genes for Archon1 (GenBank ID MG250280.1) and EGFP into the pAAV-CAG vector to obtain the final constructs (Supplementary Table 1; gene synthesis and subcloning performed by Epoch Life Science). For in vivo expression in the mouse brain via IUE, the genes encoding Archon1–KGC–EGFP–$K_V2.1_{motif}$–ER2, QuasAr3–PP–Citrine–$K_V2.1_{motif}$–ER2 (QuasAr3-s), paQuasAr3–PP–Citrine–$K_V2.1_{motif}$–ER2 (paQuasAr3-s) and CoChR–mTagBFP2–$K_V2.2_{motif}$–ER2 were subcloned into the pCAG-WPRE vector. The genes encoding QuasAr3–PP–Citrine–$K_V2.1$–ER2 and paQuasAr3–PP–Citrine–$K_V2.1$–ER2 were synthesized de novo (GenScript Biotech) based on the reported sequences[28]. The gene for CoChR–mTagBFP2–$K_V2.2_{motif}$–ER2 was assembled by Epoch Life Science using pAAV-Syn–CoChR–GFP (Addgene plasmid no. 59070) and pBAD–mTag-BFP2 (Addgene plasmid no. 34632) as the source of the genes for CoChR and mTagBFP2, respectively; the $K_V2.2$ motifs were synthesized de novo with mammalian codon optimization (Epoch Life Science). The pAAV-Syn-Archon1-KGC-EGFP-$K_V2.1_{motif}$-P2A-CoChR-$K_V2.1_{motif}$ plasmid was also cloned by Epoch Life Science. We used the Kv2.1 motif fused to CoChR for the following reason: in our original paper on soma-targeted CoChR[18], we used the KA2 sequence, which worked best with CoChR–GFP, but in this paper we used fluorophore-free CoChR, which did not express well with KA2, and rather worked better with $K_V2.1$; we also sometimes used the corresponding sequence from $K_V2.2$ as described in the text. Plasmid amplification was performed using Stellar (Clontech Laboratories) or NEB10-beta (New England BioLabs) chemically competent *Escherichia coli* cells. Small-scale isolation of plasmid DNA was performed with Mini-Prep kits (Qiagen); large-scale DNA plasmid purification was done with GenElute HP Endotoxin-Free Plasmid Maxiprep Kits (Sigma-Aldrich). The genes for ASAP3-Kv and Voltron-ST were synthesized de novo by GenScript, based on the reported sequences[5,6], and cloned into the pCAG-WPRE vector.

Neuronal culture and transfection. All mouse procedures were performed in accordance with the National Institute of Health Guide for Laboratory Animals and approved by the Massachusetts Institute of Technology Institutional Animal Care and Use and Biosafety Committees. For preparation of dissociated hippocampal mouse neuron cultures, we used postnatal day 0 or 1 Swiss Webster mice without regard to sex (Taconic Biosciences) as previously described[13]. In brief, dissected hippocampal tissue was digested with 50 units of papain (Worthington Biochemical) for 6–8 min at 37 °C, and the digestion was stopped by incubation with ovomucoid trypsin inhibitor (Worthington Biochemical) for 4 min at 37 °C. The tissue was then gently dissociated with Pasteur pipettes, and dissociated neurons were plated at a density of 20,000–30,000 per glass coverslip coated with Matrigel (BD Biosciences). Neurons were seeded in 100 μl plating medium containing MEM (Life Technologies), glucose (33 mM, Sigma), transferrin (0.01%, Sigma), HEPES (10 mM, Sigma), Glutagro (2 mM, Corning), insulin (0.13%, Millipore), B27 supplement (2%, Gibco), and heat-inactivated FBS (7.5%, Corning). After cell adhesion, additional plating medium was added. AraC (0.002 mM, Sigma) was added when glia density was 50–70% of confluence. Neurons were grown at 37 °C and 5% CO_2 in a humidified atmosphere.

For in vitro screening of candidate soma-localized Archon1 sensors, primary hippocampal neuron cultures were transfected with 500 ng plasmid DNA per well using a commercial calcium phosphate transfection kit (Life Technologies) after 4 days in vitro (DIV), as previously described[13]. After 30–60 min of incubation of cultured neurons with DNA-calcium phosphate precipitate at 37 °C, neurons were washed twice with acidic MEM buffer (pH 6.7–6.8) to remove residual calcium phosphate particles and returned to the original plating medium. All measurements on cultured neurons were taken between DIV 14 and DIV 18 (about 9–14 d post transfection) to allow sodium channel maturation (and thus spiking). No cultured neuron recordings were supplemented with all-*trans*-retinal.

Electrophysiology and fluorescence microscopy in cultured primary hippocampal neurons. Whole-cell patch-clamp recordings of cultured neurons for Supplementary Table 1 were acquired via an Axopatch 700B amplifier (Molecular Devices) and Digidata 1440 digitizer (Molecular Devices). Neurons were patched between DIV 14 and DIV 18 and were bathed in Tyrode's solution (125 mM NaCl, 2 mM KCl, 3 mM $CaCl_2$, 1 mM $MgCl_2$, 10 mM HEPES, 30 mM glucose, pH 7.3 (NaOH adjusted)) at 32 °C during measurements. Synaptic blockers (2,3-dihydroxy-6-nitro-7-sulfamoyl-benzo[f]quinoxaline (NBQX), 10 μM; D(−)-2-amino-5-phosphonovaleric acid, 25 μM; gabazine, 20 μM; Tocris) were added to the extracellular solution for single-cell electrophysiology. Borosilicate glass pipettes with an outer diameter of 1 mm and a wall thickness of 0.2 mm were pulled to produce electrodes with resistance of 3–10 MΩ and were filled with an internal solution containing 135 mM potassium gluconate, 8 mM NaCl, 10 mM HEPES, 4 mM Mg-ATP, 0.4 mM Na-GTP, 0.6 mM $MgCl_2$, 0.1 mM $CaCl_2$, pH 7.25 (KOH adjusted) at 295 mOsm. Measurements from primary neuron cultures were

performed on the electrophysiology setup described above. Patch-clamp data were acquired only if the resting potential was below −45 mV and access resistance was <25 MΩ. Access resistance was compensated at 30–70%. Fluorescence imaging was performed on an inverted fluorescence microscope (Nikon Ti), equipped with a red laser (637 nm, 100 mW, Coherent, OBIS 637LX, Pigtailed) expanded by a beam expander (Thorlabs) and focused onto the back focal plane of a 40× NA 1.15 objective lens (Nikon).

Two-photon imaging of SomArchon-expressing neurons was performed using an Olympus FVMPE-RS equipped with two lasers for fluorescence excitation. An InSight X3 laser (Spectra-Physics) tuned to 1,150 nm at 50% transmissivity was used to excite SomArchon, and a MaiTai HP Ti:Sapphire laser (Spectra-Physics) tuned to 920 nm at 15% transmissivity was used to excite EGFP. The laser beams were focused using a 25× 1.05 NA water-immersion objective lens (Olympus). SomArchon emission was separated using a 590-nm dichroic mirror and imaged with 660–750 nm and 495–540 nm filters for near-infrared and green fluorescence, respectively, and signals were collected onto separate photomultiplier tubes. Imaging was performed at 2.0 μs per pixel sampling speed with one-way galvano scanning.

Phototoxicity and photobleaching measurements in cultured neurons. For phototoxicity and photostability measurements, primary mouse neuron cultures, prepared as described above, were imaged using an inverted Eclipse Ti-E microscope (Nikon) equipped with an sCMOS camera (OrcaFlash4.2, Hamamatsu), LED light source (Spectra, Lumencor), a 637-nm laser (637 LX, OBIS) focused on the back focal plane of a 40× NA 1.15 water immersion objective lens (Nikon), and a Polygon400 Multi-wavelength Patterned Illuminator (Mightex) with a 470-nm LED (ThorLabs). To express SomArchon, neurons were infected with AAV2-CaMKII-SomArchon or AAV2-Syn-SomArchon-P2A-CoChR-$K_V2.1_{motif}$ at DIV 5. To express ASAP3-Kv and Voltron-ST, neurons were transfected with the pCAG-ASAP3-Kv-WPRE and pCAG-Voltron-ST-WPRE plasmids, respectively, using the calcium phosphate method described above. For imaging of Voltron-expressing neurons, the cells were incubated with JF525 at final concentration 1.25 μM for 60 min at 37 °C (application of higher concentrations of JF525 resulted in marked internalization of the dye within 40 min of incubation at 37 °C, thus preventing functional imaging owing to the high background fluorescence). After incubation, the cells were washed 3 times with fresh plating medium for 3 h to removed unbound dye. The reactive oxygen species (ROS) measurements were performed using CellROX Orange dye (Invitrogen) according to the manufacturer's protocol. In brief, neurons were incubated with the CellROX Orange reagent at a final concentration of 5 μM for 30 min at 37 °C in darkness, and then washed once with fresh plating medium before imaging. Immediately before imaging, cells were supplemented with the NucGreen Dead 488 reagent for detection of plasma membrane integrity, which we used to indicate cell death. Cells that showed a more than ten times increase in green fluorescence in the nucleus over background fluorescence levels were considered dead. Neurons were imaged between DIV 14 and DIV 18 in the plating medium at 22 °C. CellROX Orange fluorescence was acquired using 510/25 nm excitation at 0.8 mW/mm² and 545/40 nm emission. NucGreen fluorescence was acquired using 475/36 nm excitation at 3.5 mW/mm² and 527/50 nm emission.

IUE, AAV injection, and acute brain slice preparation. For IUE, embryonic day (E)15.5 timed-pregnant female Swiss Webster (Taconic Biosciences) mice were deeply anaesthetized with 2% isoflurane. Uterine horns were exposed and periodically rinsed with warm sterile PBS. Plasmid DNA (1–2 μg total at a final concentration of about 2–3 μg/μl diluted in sterile PBS) was injected into the lateral ventricle of one cerebral hemisphere of an embryo. Five voltage pulses (50 V, 50 ms duration, 1 Hz) were delivered using 5-mm round plate electrodes (ECM 830 electroporator, Harvard Apparatus), with the anode or cathode placed on top of the skull to target the cortex or hippocampus, respectively. Electroporated embryos were placed back into the dam, and allowed to mature to delivery. Brain slices were prepared from electroporated mice without regard to sex at postnatal day (P)12–P22.

The electroporated mice were anaesthetized by isoflurane inhalation and decapitated, and cerebral hemispheres were quickly removed and placed in cold choline-based cutting solution consisting of (in mM): 110 choline chloride, 25 $NaHCO_3$, 2.5 KCl, 7 $MgCl_2$, 0.5 $CaCl_2$, 1.25 NaH_2PO_4, 25 glucose, 11.6 ascorbic acid, and 3.1 pyruvic acid (339–341 mOsm/kg; pH 7.75 adjusted with NaOH) for 2 min, then blocked and transferred into a slicing chamber containing ice-cold choline-based cutting solution. For mice electroporated with Voltron-ST, 50 μl JF525 dye (Janelia Farm; 12.5 nM JF525 in 10 μl DMSO mixed with 10 μl Pluronic F-127 (20% w/v in DMSO; Invitrogen) and 30 μl sterile PBS) was injected into the retro-orbital sinus one day before slicing. Coronal slices (300 μm thick) were cut with a Compresstome VF-300 slicing machine, then transferred to a holding chamber with artificial cerebrospinal fluid (ACSF) containing (in mM) 125 NaCl, 2.5 KCl, 25 $NaHCO_3$, 2 $CaCl_2$, 1 $MgCl_2$, 1.25 NaH_2PO_4 and 11 glucose (300–310 mOsm/kg; pH 7.35 adjusted with NaOH), and allowed to recover for 10 min at 34 °C, followed by another 30 min at room temperature. Slices were subsequently maintained at room

temperature (22 °C) until use. Both cutting solution and ACSF were constantly bubbled with 95% O_2 and 5% CO_2.

For AAV injection, 21-day-old C57 BL/6J mice were anaesthetized with isoflurane and placed in a small animal stereotaxic apparatus (David Kopf Instruments). Animals were injected with 200 nl rAAV8-Syn-Archon1-KGC-EGFP-Kv2.1motif-ER2 using a Nanoject (Drummond Scientific) via glass pipettes with 20–30-μm diameter tips into the striatum: anteroposterior (AP) 1.2 mm, mediolateral (ML) 2.1 mm, dorsoventral (DV) 3.2 mm relative to bregma. Brain slices were then prepared from these AAV-injected mice at P30–35. Mice were deeply anaesthetized with isoflurane and perfused transcardially using cold saline containing (in mM): 194 sucrose, 30 NaCl, 4.5 KCl, 1.2 NaH$_2$PO$_4$, 0.2 CaCl$_2$, 2 MgCl$_2$, 26 NaHCO$_3$, and 10 D-(+)-glucose saturated with 95% O_2 and 5% CO_2, pH 7.4 adjusted with NaOH, 320–340 mOsm/l. Coronal slices (250–300 μm thick) were cut using a slicer (VT1200 S, Leica Microsystems) and then incubated for 10–15 min in a holding chamber (BSK4, Scientific System Design) at 32 °C with regular ACSF containing (in mM): 136 NaCl, 3.5 KCl, 1 MgCl$_2$, 2.5 CaCl$_2$, 26 NaHCO$_3$ and 11 glucose saturated with 95% O_2 and 5% CO_2, followed by at least 1 h recovery at room temperature (21–25 °C) before recording.

Concurrent electrophysiology and fluorescence imaging in acute brain slices. For the recordings shown in Fig. 1 and Extended Data Fig. 3a–c, individual slices were transferred to a recording chamber mounted on an upright microscope (Olympus BX51WI, see below) and continuously superfused (2–3 ml/min) with carbogenated ACSF at room temperature. Whole-cell patch-clamp recordings were performed with borosilicate glass pipettes (KG33, King Precision Glass) heat-polished to obtain direct current resistances of ~4–6 MΩ. For cortex recordings, pipettes were filled with an internal solution containing in mM: 120 K-gluconate, 2 MgCl$_2$, 10 HEPES, 0.5 EGTA, 0.2 Na$_2$ATP, and 0.2 Na$_3$GTP. For hippocampus and striatum recordings, pipettes were filled with an internal solution containing in mM: 131 K-gluconate, 17.5 KCl, 9 NaCl, 1 MgCl$_2$, 10 HEPES, 1.1 EGTA, 2 Na$_2$ATP, and 0.2 Na$_3$GTP. Voltage clamp recordings were made with a microelectrode amplifier (Multiclamp 700B, Molecular Devices). Cell membrane potential was held at −60 mV, unless specified otherwise. Signals were low-pass-filtered at 2 kHz and sampled at 10–20 kHz with a Digidata 1440A (Molecular Devices), and data were stored on a computer for subsequent offline analysis. Cells in which the series resistance (R_s, typically 8–12 MΩ) changed by >20% were excluded from subsequent data analysis. In addition, cells with R_s more than 25 MΩ at any time during the recordings were discarded. In some cases, conventional characterization of neurons was made in both voltage and current clamp configurations. Positive neurons were identified for recordings on the basis of EGFP expression visualized with a microscope equipped with a standard GFP filter (BX-51WI, Olympus). Optical voltage recordings were taken through a 40× water immersion objective (Olympus LUMFL N 40x/0.8W). Fluorescence was excited using a fibre-coupled 637-nm red laser (140 mW, Coherent Obis 637-140 LX), and the emission was filtered through a 664-nm long-pass filter. Images were collected on an EMCCD camera (Andor iXON Ultra 888) or sCMOS camera (Andor Zyla4.2 Plus Andor) in a reduced pixel window to enable acquisition at about 1 kHz. Each trial was about 30 s in duration. Of the 18 cortical neurons reported in Fig. 1, 4 neurons were not analysed for Fig. 1e because the electrophysiology files were inadvertently not saved, owing to a problem with the manual save process.

For optical recordings shown in Fig. 1i, j and Extended Data Figs. 1a–g, 2, 5, acute brain slices were transferred to a recording chamber mounted on an inverted Eclipse Ti-E (Nikon) equipped with a CMOS camera (Zyla5.5, Andor), LEDs (Spectra, Lumencor), a 637-nm laser (637 LX, OBIS) focused on the back focal plane of a 40× NA 1.15 objective (Nikon), and a Polygon400 Multiwavelength Patterned Illuminator (Mightex) with 470-nm LED (ThorLabs), and continuously superfused (2–3 ml/min) with carbogenated ACSF at room temperature. Positive cells were imaged under 0.8 or 1.5 W/mm^2 (55 mW) excitation light power at 637 nm from the laser. 4-Aminopyridine at a final concentration of 1 mM was added to induce neuronal activity for experiments shown in Extended Data Figs. 2c, d, g, h, 5. For Fig. 1i, j and Extended Data Fig. 5, cells were illuminated with 2-ms blue light pulses at light power in the range from 0.1 to 1.0 mW/mm^2.

Mouse surgery. All in vivo mouse procedures were performed in accordance with the National Institute of Health Guide for Laboratory Animals and approved by the Boston University Institutional Animal Care and Use and Biosafety Committees. *Virus injection surgery.* All AAVs were produced by the University of North Carolina Chapel Hill Vector Core. Adult female C57BL/6 mice (Charles River Laboratories) or Chat-cre mice (Chat-cre;129S6-Chattm2(cre)Lowl/J, the Jackson Laboratory), 8–12 weeks old at the time of surgery, were used for all experiments. AAV-Syn-SomArchon (5.9 × 10^{-12} genome copies (GC)/ml) or AAV-syn-SomArchon-P2A-CoChR-Kv2.1 (2.19 × 10^{-13} GC/ml) was injected into the motor cortex (AP: +1.5 mm, ML: ±1.5 mm, DV: −0.3 mm relative to bregma, 0.5 μl virus), visual cortex (AP: −3.6 mm, ML: ±2.5 mm, DV: −0.3 mm, 0.5 μl virus), hippocampus (AP: −2.0 mm, ML: +1.4 mm, DV: −1.6 mm, 1 μl virus) or striatum (AP: +0.8 mm, ML: −1.8 mm, DV: −2.1 mm, 1 μl virus). Viral injection

occurred at 50–100 nl/min (10 min total) using a 10-μl syringe (NANOFIL, World Precision Instruments) fitted with a 33-gauge needle (World Precision Instruments, NF33BL) and controlled by a microinfusion pump (World Precision Instruments, UltraMicroPump3–4). The syringe was left in place for an additional 10 min after injection to facilitate viral spread. About one week after the viral injection, mice underwent a second surgery to implant the cranial window for in vivo imaging. *Cortex imaging window implantation.* The imaging window consisted of a stainless steel cannula (OD: 3.17 mm, ID: 2.36 mm, height: 1 mm, AmazonSupply, B004TUE45E) fitted with a circular coverslip (no. 0, OD: 3 mm, Deckgläser Cover Glasses, Warner Instruments, 64-0726 (CS-3R-0)) adhered using a UV curable glue (Norland Products, Norland Optical Adhesive 60, P/N 6001). A craniotomy of about 3 mm in diameter was created, with the dura left intact, over the motor cortex (centred at AP: +1.5 mm, ML: ±1.75 mm) or visual cortex (AP: −3.6 mm, ML: ±2.15 mm). The imaging window was positioned over the cortex so that it was flush with the surface of the dura. Kwik-sil adhesive (World Precision Instruments, KWIK-SIL) was applied around the edges of the imaging window to hold the imaging window in place and to prevent any dental cement from touching the brain. Three small screws (J.I. Morris, F000CE094) were screwed into the skull to further anchor the imaging window to the skull. Dental cement was then gently applied to affix the imaging window to the exposed skull, and to mount an aluminium headbar posterior to the imaging window. Supplementary Fig. 1a, b provides the window placement.

Hippocampus and striatum imaging window implantation. Hippocampal and striatal window surgeries were performed in a similar way to those previously described[11,29]. For each imaging window, a virus/drug infusion cannula (26G, PlasticsOne, C135GS-4/SPC) was attached to a stainless steel imaging cannula (OD: 3.17 mm, ID: 2.36 mm, height: 1 or 2 mm, AmazonSupply, B004TUE45E). The bottom of the infusion cannula was flush with the base of the stainless steel cannula, and a circular coverslip (no. 0, OD: 3mm, Deckgläser Cover Glasses, Warner Instruments, 64-0726 (CS-3R-0)) was adhered using a UV curable glue (Norland Products, Norland Optical Adhesive 60, P/N 6001). An additional insulated stainless steel wire (diameter: 130 μm, PlasticsOne, 005SW-30S, 7N003736501F) was glued to the viral/drug infusion cannula with super glue (Henkel, Loctite 414 and Loctite 713) and protruded from the bottom of the infusion cannula and imaging window by about 200 μm for LFP recordings.

A craniotomy about 3 mm in diameter was made over the hippocampus CA1 region (AP: −2.0 mm, ML: +2.0 mm) or the striatum (AP: +0.8 mm, ML: −1.8 mm). A small notch was made on the posterior edge of the craniotomy to accommodate the infusion cannula and LFP recording electrode. The overlying cortex was gently aspirated using the corpus callosum as a landmark. The corpus callosum was then carefully thinned to expose the hippocampus CA1 region or the dorsal striatum. The imaging window was positioned in the craniotomy, and Kwik-sil adhesive (World Precision Instruments, KWIK-SIL) was applied around the edges of the imaging window to hold it in place and to prevent any dental cement from touching the brain. Three small screws (J.I. Morris, F000CE094) were screwed into the skull to further anchor the imaging window to the skull, and a small ground pin was inserted into the posterior part of the brain near the lambda suture as a ground reference for LFP recordings. Dental cement was then gently applied to affix the imaging window to the exposed skull, and to mount an aluminium headbar posterior to the imaging window. Supplementary Fig. 1c, d provides the window placement.

In mice that did not receive a virus injection before window implantation, 1 μl of AAV-syn-SomArchon (5.9 × 10^{12} GC/ml) or 1 μl of AAV-syn-SomArchon-P2A-CoChR-Kv2.1 (2.19 × 10^{13} GC/ml), or 1 μl of AAV-CAG-FLEX-SomArchon (6.3 × 10^{12} GC/ml) was injected through the virus/drug infusion cannula at 100 nl/min through an internal infusion cannula (33G, PlasticsOne, C315IS-4/SPC) connected to a microinfusion pump (World Precision Instruments, UltraMicroPump3–4), one week after the window implantation surgery. The internal infusion cannula was left in place for 10 min after injection to facilitate viral spread. Mice were awake and their heads were fixed throughout the injection period.

All mice were treated with buprenex for 48 h after surgery and single-housed to prevent any damage to the headbar or window implant.

In vivo imaging in the live mouse brain. All optical recordings were acquired on a conventional one-photon fluorescence microscope equipped with an ORCA Flash 4.0 V3 Digital CMOS camera (Hamamatsu Photonics K.K., C13440-20CU) or Hamamatsu ORCA Fusion Digital CMOS camera (Hamamatsu Photonics K.K., C14440-20UP), 10× NA0.25 LMPlanFI air objective (Olympus), 40× NA0.8 LUMPlanFI/IR water immersion objective (Olympus), 20× NA1.0 XLUMPlanFL N water immersion objective (Olympus), 16× NA0.8 CFI LWD Plan Fluorite water immersion objective (Nikon), 470-nm LED (ThorLabs, M470L3), 140-mW 637-nm red laser (Coherent Obis 637-140X), a green filter set with a 470/25-nm bandpass excitation filter, a 495-nm dichroic, and a 525/50-nm bandpass emission filter, and a near infrared filter set with a 635-nm laser dichroic filter, and a 664-nm

long-pass emission filter. The near-infrared laser illuminated a circular area of about 60–80 μm, about 80–140 μm, and about 100–200 μm in diameter in brain tissue, with FOV height (limited by camera acquisition rate) 40–60 μm, 80–100 μm, and 100–120 μm under 40×, 20×, and 16× objective lenses, respectively. A mechanical shutter (Newport, model 76995) was positioned in the laser path to control the timing of illumination over the imaging window. Optical recordings were acquired at 390–900 Hz with HCImage Live (Hamamatsu Photonics K.K.) or NIS Elements (Nikon) software. HC Image Live data were stored as DCAM image files (DCIMG), and further analysed offline in Fiji/ImageJ and MATLAB (Mathworks). NIS Elements data were stored as .nd2 files and further analysed offline using the NIS Elements software.

The GFP signal of SomArchon was acquired in the green channel ($\lambda_{ex} = 470$ nm) at $1,024 \times 1,024$ pixels with 2×2 binning to show cell structure and distribution. Optical voltage recordings were imaged in the near infrared channel ($\lambda_{ex} = 637$ nm) with 2×2 or 4×4 binning. OmniPlex system (PLEXON) was used to synchronize data acquisition from different systems. In all experiments, the OmniPlex system recorded the start of image acquisition from the sCMOS camera, the acquisition time of each frame, and other experiment-dependent signals described below.

Optical imaging of spontaneous neural activity. All in vivo optical imaging of spontaneous neural activity was performed when mice were awake with their heads fixed in a custom holder that allowed attachment of the headplate at the anterior end. Animals were covered with an elastic wrap to prevent upward movement. Spontaneous neural activity recordings lasted continuously for up to 30,000 frames (about 36 s).

Eye puff. During some in vivo hippocampal imaging recordings, an eye puff was applied to evoke high-frequency local field potential responses in the hippocampus (Extended Data Fig. 9a–d). The mice had their heads fixed in a custom holder that allowed attachment of the headplate at the anterior end, and they were covered with an elastic wrap to prevent upward movement. Each experimental session consisted of 20–30 trials, with each trial lasting for 5,000 frames (about 6 s). Three seconds after the start of image acquisition, the sCMOS camera sent a TTL pulse to a function generator (Agilent Technologies, model 33210A), which triggered a 100-ms-long air puff. The air puff was 5–10 psi, and administered via a 0.5-mm cannula placed 2–3 cm away from the eye of the mouse. The puff TTL pulses were also recorded with the OmniPlex system (PLEXON). Eye movement was monitored using a USB webcam (Logitech, Carl Zeiss Tessar 2.0/3.7 2MP Autofocus).

Optopatch blue light stimulation. All in vivo optopatch (that is, optogenetics plus voltage imaging) experiments were performed when mice were awake with their heads fixed in a custom holder that allowed attachment of the headplate at the anterior end. Mice were covered with an elastic wrap to prevent upward movement. A 470-nm LED (ThorLabs, M470L3) was coupled to a Polygon400 Multiwavelength Patterned Illuminator (Mightex), and the blue light was focused through the objective lens to illuminate the centre of the FOV. At the onset of imaging, the sCMOS camera sent a TTL pulse to trigger Axon CNS (Molecular Devices, Digidata 1440A) which controlled the 470-nm LED (ThorLabs). Each trial lasted 1.1 s and consisted of a single 100-ms-long blue light pulse, 500 ms after trial onset. Each recording session consisted of 10 trials with increasing blue light power from 0.1 to 1 mW/mm^2, with a step of about 0.1 mW/mm^2 per trial. The OmniPlex system (PLEXON) recorded the timing of TTL pulses used to trigger the Axon CNS.

Head-fixed voluntary movement experiments. All voluntary movement experiments were performed while awake, head-fixed mice were freely navigating a spherical treadmill. The spherical treadmill was constructed as described[30]. In brief, a 3D spherical Styrofoam ball was supported by air, and motion was tracked using two computer mouse sensors positioned roughly ±45° from the centre along the equator of the ball. All motion-sensor displacement data were acquired at 100 Hz on a separate computer and synthesized using a custom Python script. Motion sensor displacement data were then sent to the image acquisition computer to be accumulated using a modified ViRMEn MATLAB script. The timing of each motion sensor displacement data point was also recorded using the OmniPlex system (PLEXON) to synchronize movement data with optical voltage recordings.

To determine the mouse movement speed, ball movement was first calibrated. The ball was pinned on the two sides and rotated vertically to calibrate sensor displacement.

All mice were habituated on the spherical treadmill for at least 3 days, at least 20 min per day, before image acquisition. During optical imaging, mice were imaged while freely navigating the spherical treadmill. Each FOV was recorded for at least 36 s in total. In some fields of view, we performed multiple trials, and each trial was at least 12 s in duration with an inter-trial interval of at least 30 s in duration.

Local field potential recording. Local field potentials were recorded using an OmniPlex system (PLEXON) at a 1 kHz sampling rate. To synchronize optical recordings with LFP recordings, the camera sent out a TTL pulse to the OmniPlex system at the onset of imaging and after each acquired frame.

Motion correction. In Figs. 2i, 3, 4, motion correction was performed with a custom Python script. For FOV, if multiple video imaging files were collected for the same FOV, we started with the first imaging file to ensure speedy data processing (a single video file contains a series of images). We first generated the reference image by averaging across all images within the file. We then performed a series of image processing procedures to enhance the contrast of the reference image and every image in the file to facilitate motion correction. We first removed 10% of the pixels along all edges of an image to remove any camera induced artefact. We then applied a high-pass filter (Python scipy package, ndimage.gaussian_filter, sigma = 50) to remove low-frequency components within the images. To enhance the boundaries of high intensity areas, we identified the boundaries as the difference between two low-pass-filtered images (sigma = 2 and 1). We then enhanced the boundary by adding 100 times the boundary back to the low-pass-filtered image (sigma = 2). We then limited the intensity range of the processed images within one standard deviation above and below the average intensity of the image, by setting the pixels with intensity higher than mean + s.d. as mean + s.d., and the pixels with intensity lower than mean − s.d. as zero. Finally, to counter any potential bleaching over time, we normalized the intensity of each image by shifting the mean intensity to zero and divided intensity values by the s.d. of all pixel intensities in that image. After image processing, we calculated the displacement of each image, by identifying the maximum cross-correlation coefficient between each image and the reference image, and then corrected motion by shifting the displacement in the original, unenhanced image sequence. If the same FOV was imaged over an extended period of time, during which multiple files were acquired, we motion-corrected subsequent files by aligning them to the first file, so that the same ROIs from the same FOV could be applied across the entire imaging session. Specifically, we first refined the reference frame by generating the mean intensity projection image from the motion-corrected first imaging file. The refined reference image was then used to motion-correct all files of the same FOV, including the first file, using the procedure described above. The motion-corrected, original, unenhanced image sequences were then used for subsequent manual ROI segmentation and further analysis.

ROI identification. We imported the image files (motion-corrected as above, if necessary) into Fiji/ImageJ or NIS Elements and manually segmented ROIs by examining the time-series images to identify areas with clear neuron outlines and/or intensity dynamics over time. The optically recorded voltage traces for each ROI were generated from the motion-corrected image sequences using the multiple measurement function and were used for analyses.

The wide dynamic range (16 bit) of the raw images meant that to select dim as well as bright cells, we had to create maximum projection and standard deviation images of the entire raw video, and stretched their look-up tables to enhance visibility. For Fig. 4 and Extended Data Fig. 9e–h, cells were densely packed, so we identified and tracked ROIs semi-manually across image sequences without performing motion correction. We first visually inspected all image sequences and identified those with minimal motion and with an SNR greater than about 2 for further analysis. We then performed an iterative ROI-selection procedure to identify ROIs that best fit each cell. Specifically, we started by manually selecting ROIs from the maximum projection image of the entire image sequence. The image sequence was then visually inspected to identify frames with cells that exhibited shifts of more than three pixels from the defined ROI. We then used these frames to separate the image sequence into multiple time intervals, and obtained a new set of maximum projection images to identify new ROIs within these time intervals for these cells. This procedure was repeated iteratively until the ROI represented the cell across all image frames in their corresponding time intervals without the cell moving out of the ROI. Thus, with this procedure, we created multiple ROIs representing the same cell across different frames. For each cell, we extracted traces for every ROI during its corresponding time interval, and stitched the baseline-normalized traces for the same cell(s) in time. The fluorescence traces of each cell were then detrended for further analysis. Supplementary Fig. 2 provides an example of raw and processed traces for two cells in the same FOV.

Hippocampal spike detection. Spikes were associated with a rapid increase in intensity, followed by a rapid decrease. By contrast, occasional motion artefacts were usually associated with a decrease in intensity as a neuron moved out of the ROI. To facilitate spike detection, we first removed motion artefacts. For each time point of the fluorescence intensity trace for each ROI, we calculated the change in intensity from that of the prior time point (I_{change}). We then defined noise as the time points at which instantaneous I_{change} was 3 s.d. below the mean value of I_{change} across the entire trace. We excluded any time points at which the I_{change} of the previous time point was more than 1 s.d. above the average I_{change}, because this might have indicated a spike. These noise time points and their following three time points (as we found that motion artefacts are typically >4 ms) were then considered motion artefacts, and removed from further analysis. We then recalculated the standard deviation of I_{change}, excluding the data points related to the motion artefact. The peaks of spikes were then identified as time points that

met the following two criteria: (1) the intensity change of the time point combined with that of its preceding time point was more than 3 s.d. above the average I_{change}, and (2) the intensity change over the next two time points was less than 2 s.d. below the average I_{change}.

Hippocampal spike–phase calculation. Hippocampal spike–phase analysis was performed on 16 neurons from 7 FOVs in 4 mice. For each FOV, we analysed data collected over 10 trials (about 60 s in total) during which animals experienced an eye puff in each trial, as described above. To calculate the phase of spikes at theta frequency (4–10 Hz), we first band-pass-filtered both the optical voltage trace and the simultaneously recorded LFP at theta frequency (eegfilt, EEGLAB toolbox). The peaks of theta oscillation power were then identified using the findspike function in MATLAB. For each spike, we obtained the phase of the spike by calculating the timing of each spike relative to the period of that oscillation cycle in degrees. We averaged the phases of all spikes from the same neuron as the average phase of a given neuron.

Analysis for pairwise coherence between hippocampal neurons and LFPs. The coherence analysis was performed on nine FOVs that contained multiple neurons from four mice. Each FOV contained imaging data over a period of 6–36 s. For each FOV, we first re-sampled the LFP at the acquisition rate of the optical imaging. We then divided the optical voltage traces and LFPs into segments of 1,000 data points. We then calculated the averaged coherence, at theta frequency (4–10 Hz), with the functions in the Chronux toolbox (optical voltage trace to optical voltage trace or LFP: coherencyc, and spike to spike: coherencypt) with tapers = [10 19], fpass = [4 10] and trialave = 1. To compare V_{mo}–V_{mo} coherence with V_{mo}–LFP coherence across nine FOVs, we averaged the coherence of neurons in the same FOV to obtain the mean coherence of that FOV, and then performed statistical tests across FOVs using the mean coherences of the individual FOVs. To understand the relationships between pairs of coherence, we used the MATLAB function fitlm to perform a linear regression between coherent pairs and obtain the P and r^2 values.

To estimate background fluorescence crosstalk, we calculated pairwise coherence and correlation between background doughnut areas surrounding a neuron. To select background doughnut areas, we excluded the edges (5%) of each FOV, because the edge may be missing for a particular image frame when image frames were shifted during motion correction. The background doughnut of a neuron was determined as the area 3–10 μm from the neuron boundary, excluding any pixels within 10 μm of the boundary of another neuron. One neuron was excluded from this analysis owing to dense labelling where we could not identify its doughnut area. Fluorescence traces of the background doughnut area were then processed as for neurons, and their pairwise coherence and Pearson correlations were calculated.

Spike detection for striatum, motor cortex, and visual cortex. After motion correction, we first identified large fluorescence increases using a threshold of 4 s.d. above the baseline. The baseline was manually selected as a period of >500 ms without spiking or drifting due to z-plane shifting or photobleaching. From these large fluorescence increases, we selected those with rise times and decay times shorter than 4 ms as spikes.

Firing rate comparison of striatal neurons during high- and low-speed movement. Movement data of mice were first interpolated to the voltage imaging frame rate with MATLAB function interp1, and then smoothed using a 1.5-Hz low-pass Butterworth filter to remove any motion sensor artefacts. We calculated the average movement speed at 0.5-s intervals and defined low-speed periods as intervals during which the average speed was ≤5 cm/s and high-speed periods as intervals during which the average speed was ≥10 cm/s. The firing rates during these high- and low-speed motion periods were compared, and a two-sided Wilcoxon rank-sum test was used to identify significant differences between these periods.

SNR calculation for in vivo photostability evaluation over imaging duration in striatum and hippocampus. We defined noise as the standard deviation of the fluorescence intensity across the entire trial period. For each neuron, we first calculated the SNR for each action potential by dividing the intensity change observed during an action potential by the noise, and then calculated the average SNRs across all spikes detected in a trial as the corresponding SNR for the trial. For the striatum dataset, only neurons imaged over at least five consecutive trials were analysed. For the hippocampus dataset, all neurons were analysed.

Detrending. All optically recorded SomArchon traces reported in the manuscript (except those shown in Fig. 4a–d) were corrected for photobleaching or focus shift by subtracting baseline fluorescence traces that were low-pass-filtered and fit to a double or single exponential function.

Histology. Mice were transcardially perfused with PBS followed by 4% paraformaldehyde. The brain was gently extracted from the skull and post-fixed in 4% paraformaldehyde for 1–4 h at room temperature or overnight at +4 °C. Fixed brains were transferred to a 30% sucrose–PBS solution and rotated for 24–48 h at 4 °C for cryoprotection. Cryoprotected brains were frozen in OCT in a dry ice bath and sliced (coronally) to 50-μm thickness using a cryostat. Glial and microglial antibody staining were performed with anti-GFAP[29] (1:250, Clone N206/A8, Neuromab) and anti-IBA1[31] (1:500, 019-19741, Wako Chemicals) primary

antibodies, respectively, followed by Alexa Fluor 568 (1:1,000, goat anti-mouse IgG (H+L) cross-adsorbed secondary antibody, A11004, InVitrogen) and 633 secondary antibodies (1:1,000, goat anti-rabbit IgG (H+L) cross-adsorbed secondary antibody, A21070, InVitrogen). All antibodies were used according to protocols that have been validated by their suppliers. Slice imaging was performed using an inverted Nikon Eclipse Ti microscope equipped with a spinning disk sCSUW1 confocal scanner unit (Yokogawa), 488-, 561-, and 642-nm solid state lasers, 525/25-nm, 579/34-nm, and 664LP emission filters, a 20× NA0.75 air objective lens (Nikon), and a 4.2 PLUS Zyla camera (Andor), controlled by NIS-Elements AR software. Acquired images were contrast-enhanced to improve visualization.

Brain temperature measurements. Under general anaesthesia, a craniotomy about 3 mm in diameter was made to expose the brain surface, with a small notch on the posterior edge to accommodate the insertion of a temperature probe (Physitemp, IT-1E) coupled to a Thermocouple DAQ (DATAQ Instruments, Model DI-245). An imaging window, identical to those used in all imaging experiments, was positioned on the craniotomy. Kwik-sil adhesive was applied around the edges of the imaging window to hold it in place, but not around the craniotomy notch, to allow insertion of the temperature probe. Dental cement was then gently applied to affix the imaging window to the skull and to mount an aluminium headbar. Once mice had recovered from anaesthesia, they had their heads fixed while awake and the temperature probe was inserted under the imaging window above the brain surface, through the craniotomy notch. The 637-nm laser was directed through the 40× objective under identical conditions to those used while imaging (75–95 mW laser power), and brain temperature was recorded. We noted a temperature increase of 1.88 ± 0.80 °C (mean ± s.d., $n = 3$ mice) over the 12-s illumination period commonly used in our experiments. These changes are similar to, or smaller than, changes commonly seen with two-photon imaging, optogenetics, and the making of craniotomies for neural imaging[32–36].

Sample size. No statistical methods were used to estimate sample size for mouse studies throughout. We did not perform a power analysis, as our goal was to create a new technology, as recommended by the NIH: "In experiments based on the success or failure of a desired goal, the number of animals required is difficult to estimate…"[37]. As noted in the aforementioned paper, "The number of animals required is usually estimated by experience instead of by any formal statistical calculation, although the procedures will be terminated [when the goal is achieved]." These numbers reflect our past experience in developing neurotechnologies.

Data exclusions. Voltage imaging datasets with significant motion or in which no spikes were detected were excluded from analysis. Significant motion was defined as a shift of more than 20 μm in any direction. In Extended Data Fig. 1i–k, data points that corresponded to overlapping neurites were excluded. Data exclusion criteria were not pre-established.

Replication. All attempts at replication were successful.

Randomization and blinding. There were no treatment conditions to compare in this study. All recording sessions were randomly performed with different voltage sensors or in different brain regions. On recording days, cultured cells or brain slices expressing specific sensors were known. On in vivo recording days, mouse conditions were known. Voltage trace extraction and subsequent analysis were performed with the investigators unaware of specific mouse conditions. For analysis of movement modulation of striatal neuron spiking, a computer algorithm was used to identify periods with different movement parameters. For analysis of spike–phase relationships, or subthreshold membrane voltage relationships, a computer algorithm was used across all conditions. For histology, sections were selected and images were taken from slides by a researcher not aware of the conditions or antibody used. Cells were also counted and quantified from these sections by a researcher blinded to the experimental conditions or antibody used.

Reporting summary. Further information on research design is available in the Nature Research Reporting Summary linked to this paper.

Code availability

Computer code used to generate results for this study is available at https://github.com/HanLabBU/somarchon-imaging.

Data availability

The data that support the findings of this study are available from the corresponding author upon reasonable request; raw data essential to the work are available online as Source Data files. Sequences of the reported proteins are available at GenBank at the following accession codes: SomArchon MN091368; SomArchon-P2A-CoChR-K$_V$2.1$_{motif}$, MN091369.

28. Adam, Y. et al. Voltage imaging and optogenetics reveal behaviour-dependent changes in hippocampal dynamics. *Nature* **569**, 413–417 (2019).
29. Hansen, K. R. et al. Mild blast injury produces acute changes in basal intracellular calcium levels and activity patterns in mouse hippocampal neurons. *J. Neurotrauma* **35**, 1523–1536 (2018).

30. Dombeck, D. A., Khabbaz, A. N., Collman, F., Adelman, T. L. & Tank, D. W. Imaging large-scale neural activity with cellular resolution in awake, mobile mice. *Neuron* **56**, 43–57 (2007).
31. Fields, I. E. et al. Noninvasive deep brain stimulation via temporally interfering electric fields. *Cell* **169**, 1029–1041.e16 (2017).
32. Kalmbach, A. S. & Waters, J. Brain surface temperature under a craniotomy. *J. Neurophysiol.* **108**, 3138–3146 (2012).
33. Podgorski, K. & Ranganathan, G. Brain heating induced by near-infrared lasers during multiphoton microscopy. *J. Neurophysiol.* **116**, 1012–1023 (2016).
34. Arias-Gil, G., Ohl, F. W., Takagaki, K. & Lippert, M. T. Measurement, modeling, and prediction of temperature rise due to optogenetic brain stimulation. *Neurophotonics* **3**, 045007 (2016).
35. Stujenske, J. M., Spellman, T. & Gordon, J. A. Modeling the spatiotemporal dynamics of light and heat propagation for in vivo optogenetics. *Cell Rep.* **12**, 525–534 (2015).
36. Christie, I. N. et al. fMRI response to blue light delivery in the naïve brain: implications for combined optogenetic fMRI studies. *Neuroimage* **66**, 634–641 (2013).
37. Dell, R. B., Holleran, S. & Ramakrishnan, R. Sample size determination. *ILAR J.* **43**, 207–213 (2002).

Author contributions K.D.P. and E.S.B. initiated the project. K.D.P., S.B., H.T., S.N.S., X.H., and E.S.B. designed all in vivo experiments and interpreted the data. K.D.P. developed SomArchon and together with E.E.J., O.A.S., and E.C. characterized all constructs in cultured cells. K.D.P., V.G.L.-H., D.P., C.S., Z.F., and B.L.S. performed characterization of SomArchon in acute brain slices. S.B., S.N.S. and H.J.G. performed all mouse surgeries for in vivo experiments. M.F.R. assisted on imaging setups. K.D.P., S.B., H.T., and S.N.S performed all in vivo imaging experiments and analysed all in vivo imaging data. K.D.P., S.B., H.T., S.N.S, X.H. and E.S.B. wrote the paper with contributions from all of the authors. E.S.B. and X.H. oversaw all aspects of the project.

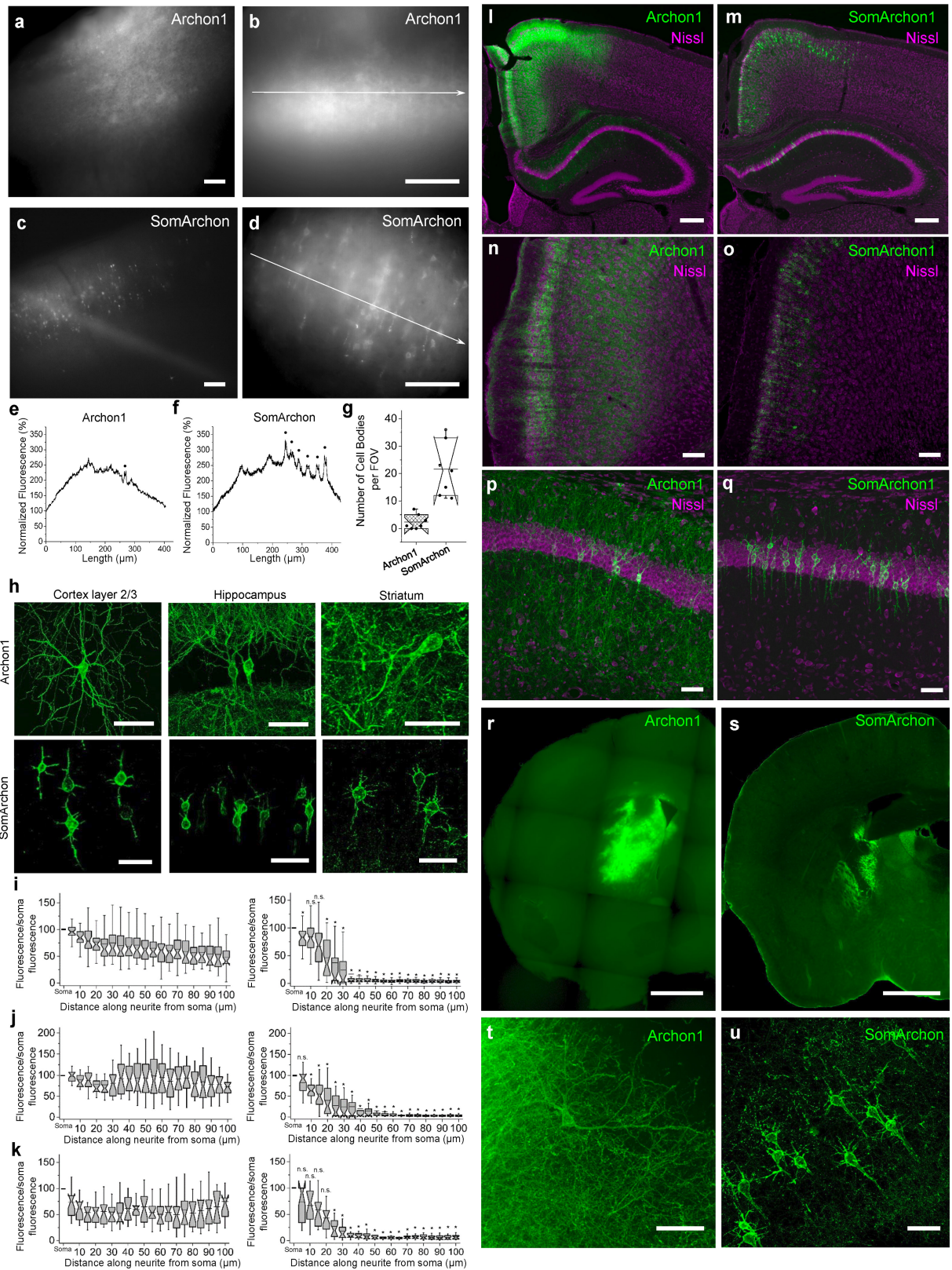**Competing interests** The authors declare no competing financial interests.

Additional information
Supplementary information is available for this paper at https://doi.org/10.1038/s41586-019-1641-1.
Correspondence and requests for materials should be addressed to E.S.B. or X.H.
Peer review information *Nature* thanks Kenneth Harris, Lin Tian, Christian Wilms and the other, anonymous, reviewer(s) for their contribution to the peer review of this work.
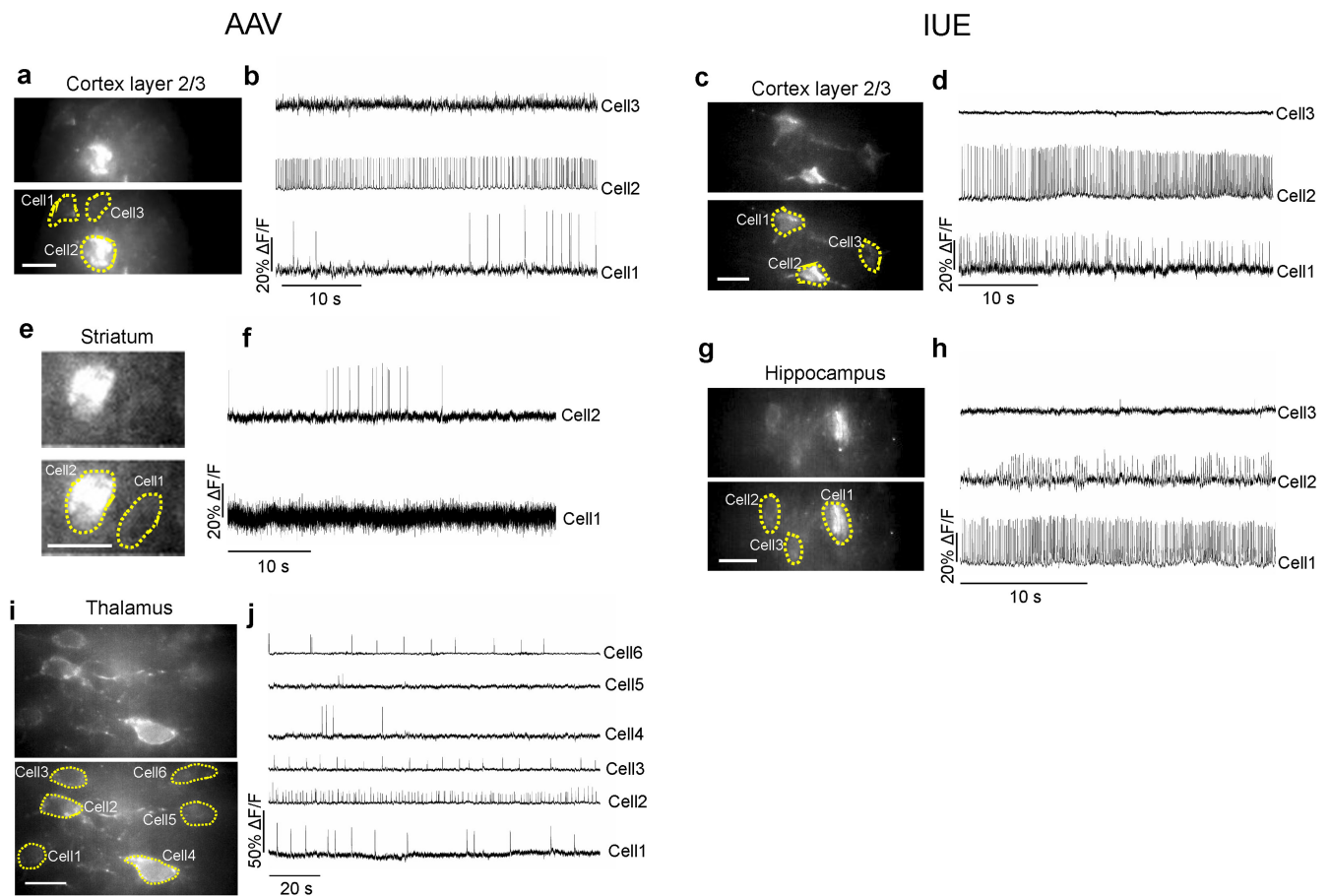**Reprints and permissions information** is available at http://www.nature.com/reprints.

Extended Data Fig. 1 | See next page for caption.

Extended Data Fig. 1 | Expression of Archon1 and SomArchon in mouse brain. a–d, Representative images of mouse brain slices expressing Archon1 (**a**, **b**) and SomArchon (**c**, **d**) (CAG promoter, via IUE) imaged with a wide-field microscope with $10\times$ (**a**, **c**) and $40\times$ (**b**, **d**) objective lenses (from $n = 7$ slices from 2 mice each). **e**, **f**, Normalized EGFP fluorescence along white arrows shown in **b**, **d**, respectively. Black dots correspond to resolvable cells. **g**, Number of resolvable cells per FOV for brain slices expressing Archon1 or SomArchon (2.4 ± 2.5 and 22 ± 9 neurons per FOV ($350 \times 415\,\mu m^2$) for Archon1 and SomArchon, respectively). Mean $\pm$ s.d.; $n = 7$ slices from 2 mice each; box plots as in Fig. 1. Further confocal analysis with larger FOVs of $500 \times 500 \times 50\,\mu m^3$ revealed that SomArchon can resolve around 15 times more neurons in the cortex than Archon1 ($n = 4, 8, 9, 11, 11, 18$, and 20 neurons from 7 slices for Archon1, versus $n = 180, 187$, and 137 neurons from 3 slices for SomArchon). **h**, Representative con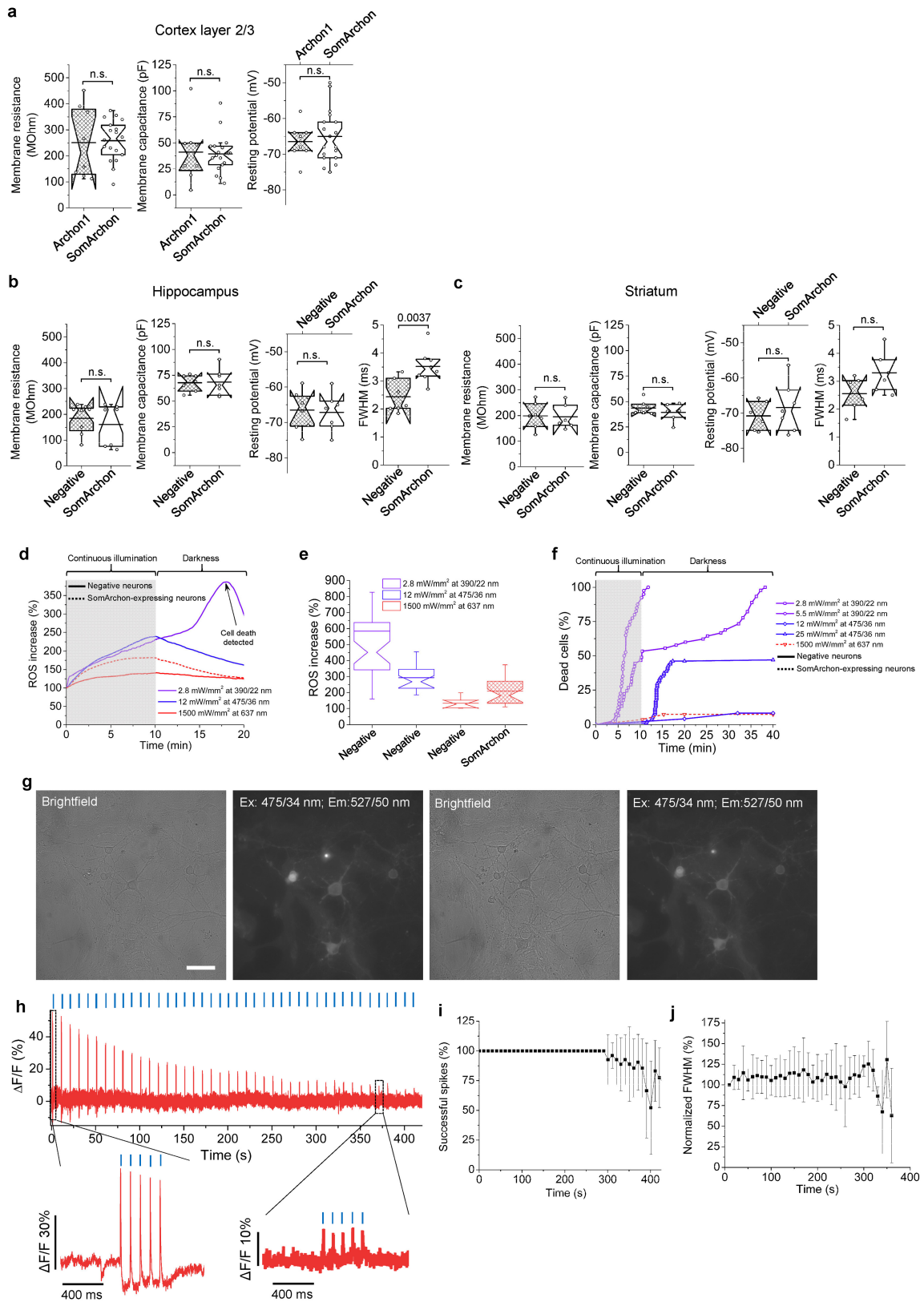focal images of neurons in cortex layer 2/3 (left), hippocampus (middle), and striatum (right) expressing Archon1 (top) and SomArchon (bottom). **i–k**, EGFP fluorescence along a neurite, normalized to soma, for neurons expressing Archon1 (left) or SomArchon (right) in cortex layer 2/3 (**i**, $n = 39$ and 37 neurites from 10 cells from 2 mice each), hippocampus (**j**, $n = 20$ and 34 neurites from 9 and 17 cells from 2 mice each), and striatum (**k**, $n = 17$ and 20 neurites from 7 cells from 2 mice each). Box plots as in Fig. 1. $*P < 0.002$ compared to Archon1 at corresponding position away from the soma; n.s., not significant. Two-sample Kolmogorov–Smirnov test, see Supplementary Table 2. **l–u**, Representative confocal fluorescence images of brain slices expressing Archon (left) or SomArchon (right) via IUE (**l–q**) or AAV injection (**r–u**) in cortex layer 2/3 (**n**, **o**; $n = 8$ slices from 2 mice), hippocampus (**p**, **q**; $n = 8$ slices from 2 mice), and striatum (**t**, **u**; $n = 6$ slices from 2 mice). Green, EGFP; magenta, Nissl staining. Scale bars, $100\,\mu m$ (**a–d**), $50\,\mu m$ (**h**, **n–q**, **t**, **u**), $250\,\mu m$ (**l**, **m**, **r**, **s**).

Extended Data Fig. 2 | Voltage imaging using SomArchon in mouse brain slices. a–d, Representative fluorescence wide-field images of cortex layer 2/3 neurons expressing SomArchon via AAV transduction (**a**) or IUE (**c**) with selected ROIs (bottom), and corresponding fluorescence traces (**b, d**; $n = 6$ and 13 slices from 2 and 4 mice for AAV transduction and IUE, respectively). Acquisition rate, 632 Hz (**b**) or 440 Hz (**d**). **e, f**, Representative fluorescence wide-field images of striatal neurons expressing SomArchon via AAV transduction (top) with selected ROIs (bottom) (**e**), and corresponding fluorescence traces (**f**; $n = 8$ slices from
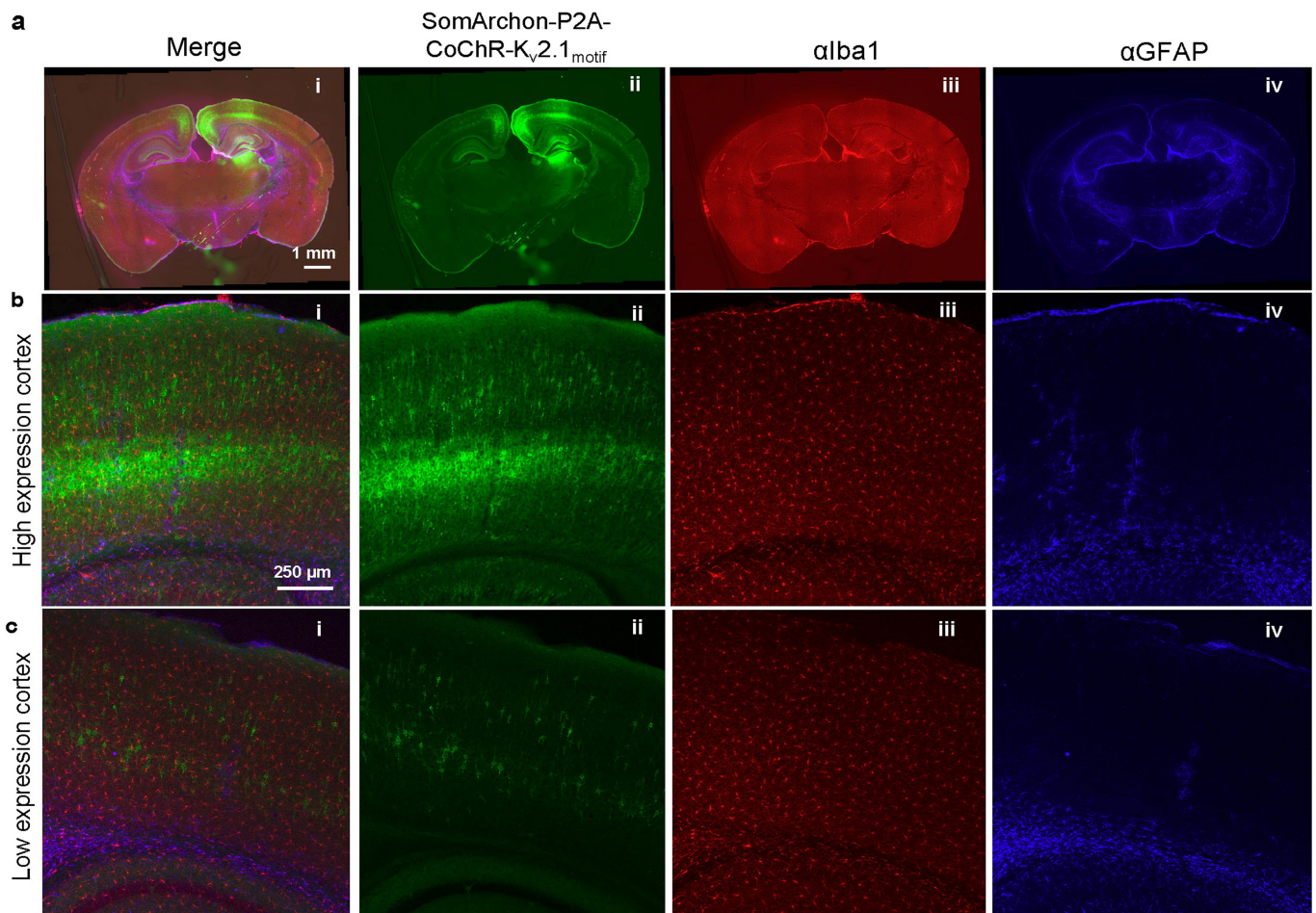
2 mice). Acquisition rate, 733 Hz. **g, h**, Representative fluorescence wide-field images of hippocampal neurons expressing SomArchon via IUE (top) with selected ROIs (bottom) (**g**), and corresponding fluorescence traces (**h**; $n = 8$ slices from 2 mice). Acquisition rate, 333 Hz. **i, j**, Fluorescence wide-field images of thalamus neurons expressing SomArchon (top) via AAV transduction with selected ROIs (bottom) (**i**), and corresponding fluorescence traces (**j**; $n = 5$ slices from 2 mice). Acquisition rate, 333 Hz. Scale bars, 25 μm.
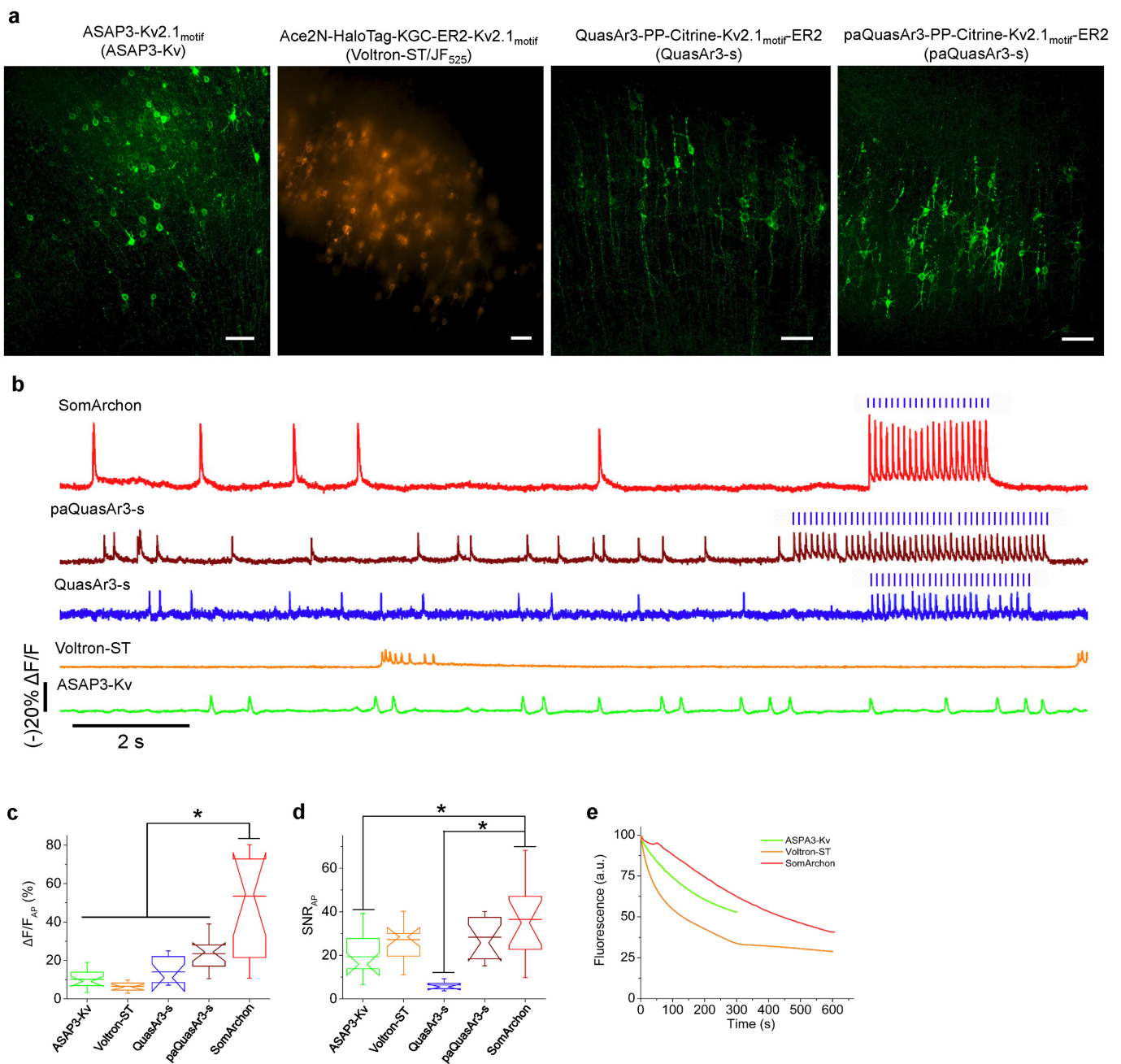
Extended Data Fig. 3 | See next page for caption.

Extended Data Fig. 3 | Expression of SomArchon and voltage imaging do not alter membrane properties or cause phototoxicity. a, Membrane properties of neurons expressing Archon (hashed boxes) or SomArchon (open boxes) in cortex layer 2/3 brain slices ($P = 0.8026$, 0.8895, and 0.8236 for resistance, capacitance, and resting potential, respectively; two-sided Wilcoxon rank-sum test comparing Archon1 versus SomArchon; $n = 8$ and 18 cells from 1 and 2 mice for Archon1 and SomArchon, respectively). **b**, Similar to **a** but in hippocampus ($P = 0.6294$, 0.9720, 0.8880, and 0.0037 for resistance, capacitance, resting potential, and FWHM, respectively; two-sided Wilcoxon rank-sum test comparing negative versus SomArchon; $n = 8$ and 7 cells from 2 mice each for negative and SomArchon for resistance and resting potential; $n = 7$ and 7 cells from 2 mice each for negative and SomArchon for capacitance; $n = 7$ and 8 cells from from 2 mice each for negative and SomArchon for FWHM). **c**, Similar to **a** but in striatum ($P = 0.7380$, 0.8357, 0.7751, and 0.0931 for resistance, capacitance, resting potential and FWHM, respectively; two-sided Wilcoxon rank-sum test comparing negative and SomArchon; $n = 7$ and 6 cells from 2 mice each for negative and SomArchon for resistance and capacitance; $n = 6$ and 7 cells from 2 mice each for negative and SomArchon for resting potential; $n = 6$ and 6 cells from 2 mice each for negative and SomArchon for FWHM). **d**, Changes in relative ROS concentration (normalized to that before illumination) over time in negative (solid line) and SomArchon-expressing (dashed line) cultured mouse neurons under various illumination protocols.

e, Maximal increase in ROS concentration during continuous illumination for conditions performed in **d** ($n = 45$, 24, and 8 negative neurons from 2, 2, and 1 cultures for 390/22 nm, 475/36 nm, and 637 nm illumination, respectively; $n = 24$ SomArchon-expressing neurons for 637 nm illumination from 1 culture). **f**, Cell death for negative (solid line) and SomArchon-expressing (dashed line) cultured neurons at DIV 14–18 under various illumination protocols ($n = 45$, 35, 91, 40, and 27 neurons from 2, 1, 2, 1, and 1 cultures, respectively, for 390/22 nm at 2.8 mW mm^{-2}, 390/22 nm at 5.5 mW mm^{-2}, 475/36 nm at 12 mW mm^{-2}, 475/36 nm at 25 mW mm^{-2}, and 637 nm at 1,500 mW mm^{-2} illumination). **g**, Bright-field and fluorescence images of representative neurons expressing SomArchon before and after 10 min of continuous 637-nm laser illumination at 1,500 mW mm^{-2}, followed by 10 min in darkness (93% of imaged cells did not exhibit noticeable changes in morphology; $n = 27$ cells from 1 culture; non-illuminated cells did not show any changes in morphology; $n = 10$ cells from 1 cultures). Scale bar, 50 μm. **h**, Representative SomArchon fluorescence trace from neuron co-expressing SomArchon and CoChR-K$_v$2.1$_{motif}$. **i**, Normalized spike rates (to initial value) elicited by blue light illumination dropped after 300 s of continuous recording, owing to decrease in spike amplitude as a result of photobleaching ($n = 10$ neurons from 1 culture; plotted as mean ± s.d.). **j**, Normalized (to initial value) FWHM of spikes elicited by continuous light exposure as in **h**. Box plots as in Fig. 1.
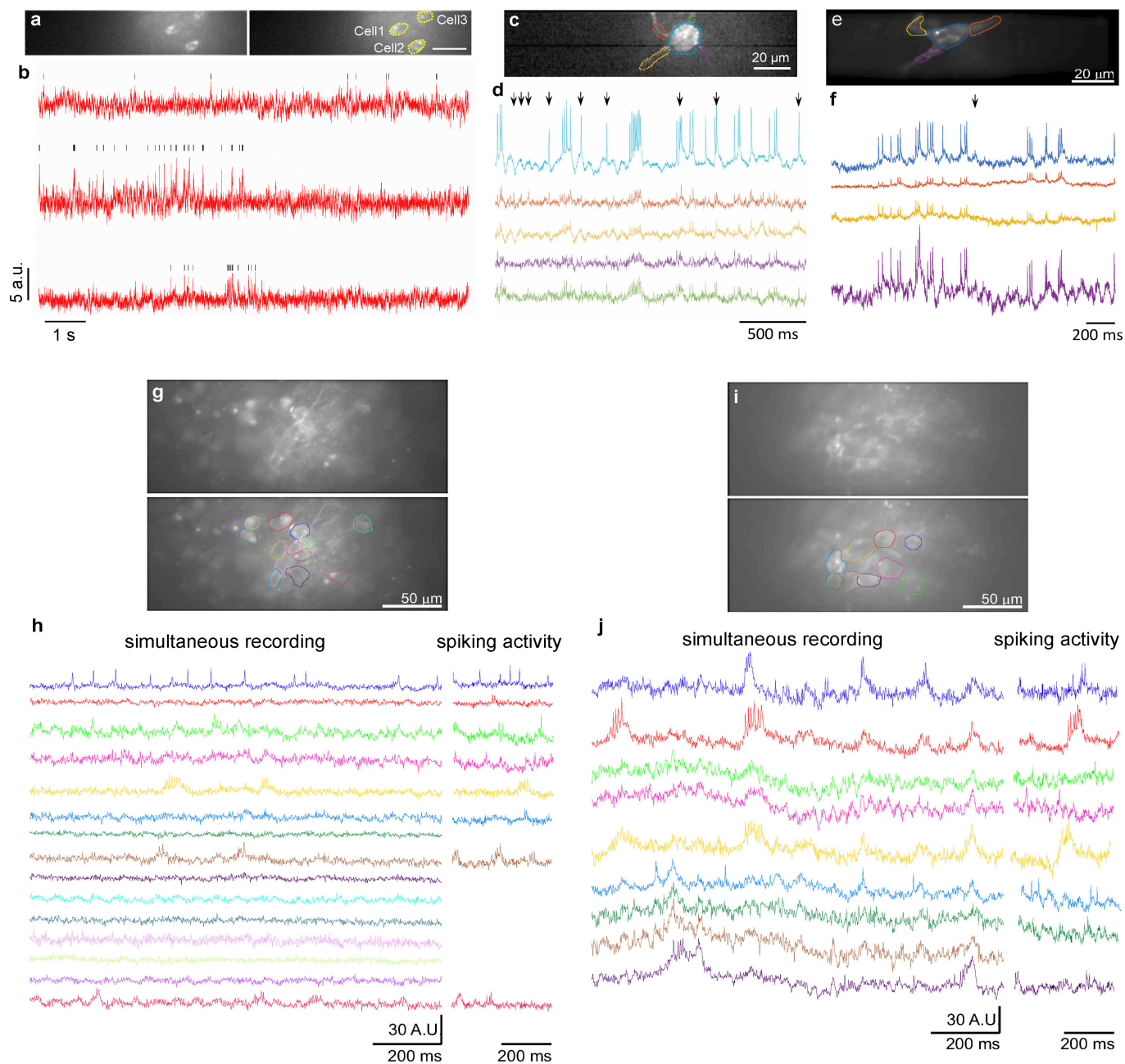
Extended Data Fig. 4 | SomArchon expression in vivo does not cause gliosis. SomArchon was expressed in the mouse brain by AAV2.9-Syn-SomArchon-P2A-CoChR-$K_V2.1_{motif}$ injection into the cortex in P0 Swiss Webster mice. Brain tissues were analysed 63 days after viral injection. Merged fluorescence images from 50-μm-thick coronal sections (i) were visualized via EGFP fluorescence of SomArchon (ii), anti-IBA1 immunofluorescence (iii), and anti-GFAP immunofluorescence (iv; $n = 4$ slices from 2 mice). **a**, Expression throughout the coronal section. **b**, Zoomed-in view of the virally injected area (high-expression cortex). **c**, Zoomed-in view of the non-injected contralateral hemisphere (low-expression cortex). The commonly used glial and microglial markers GFAP and IBA1 appeared similarly in both hemispheres, suggesting that expression of SomArchon did not cause gliosis. Scale bars, 1 mm (**a**), 250 μm (**b**, **c**).

Extended Data Fig. 5 | Side-by-side comparison of next-generation voltage indicators in mouse brain slices. a, Representative fluorescence images of mouse cortex layer 2/3 neurons expressing ASAP3-K_V2.1$_{motif}$ (ASAP3-Kv), Ace2N-HaloTag-KGC-ER2-K_V2.1$_{motif}$ (Voltron-ST/JF$_{525}$), QuasAr3-PP-mCitrine-K_V2.1$_{motif}$-ER2 (QuasAr3-s), and paQuasAr3-PP-mCitrine-K_V2.1$_{motif}$-ER2 (paQuasAr3-s). ASAP3-Kv, QuasAr3-s and paQuasAr3-s were visualized via cpGFP, mCitrine, and mCitrine fluorescence, respectively, using laser excitation at 488 nm and emission at 525/50 nm under a confocal microscope. Voltron-ST/JF$_{525}$ was visualized via JF525 fluorescence using LED excitation at 510/25 nm and emission at 545/40 nm under a wide-field microscope. Scale bar, 50 μm. **b**, Single-trial optical recordings of ASAP3-Kv (green) and Voltron-ST/JF$_{525}$ (orange) fluorescence responses during neuronal activity evoked
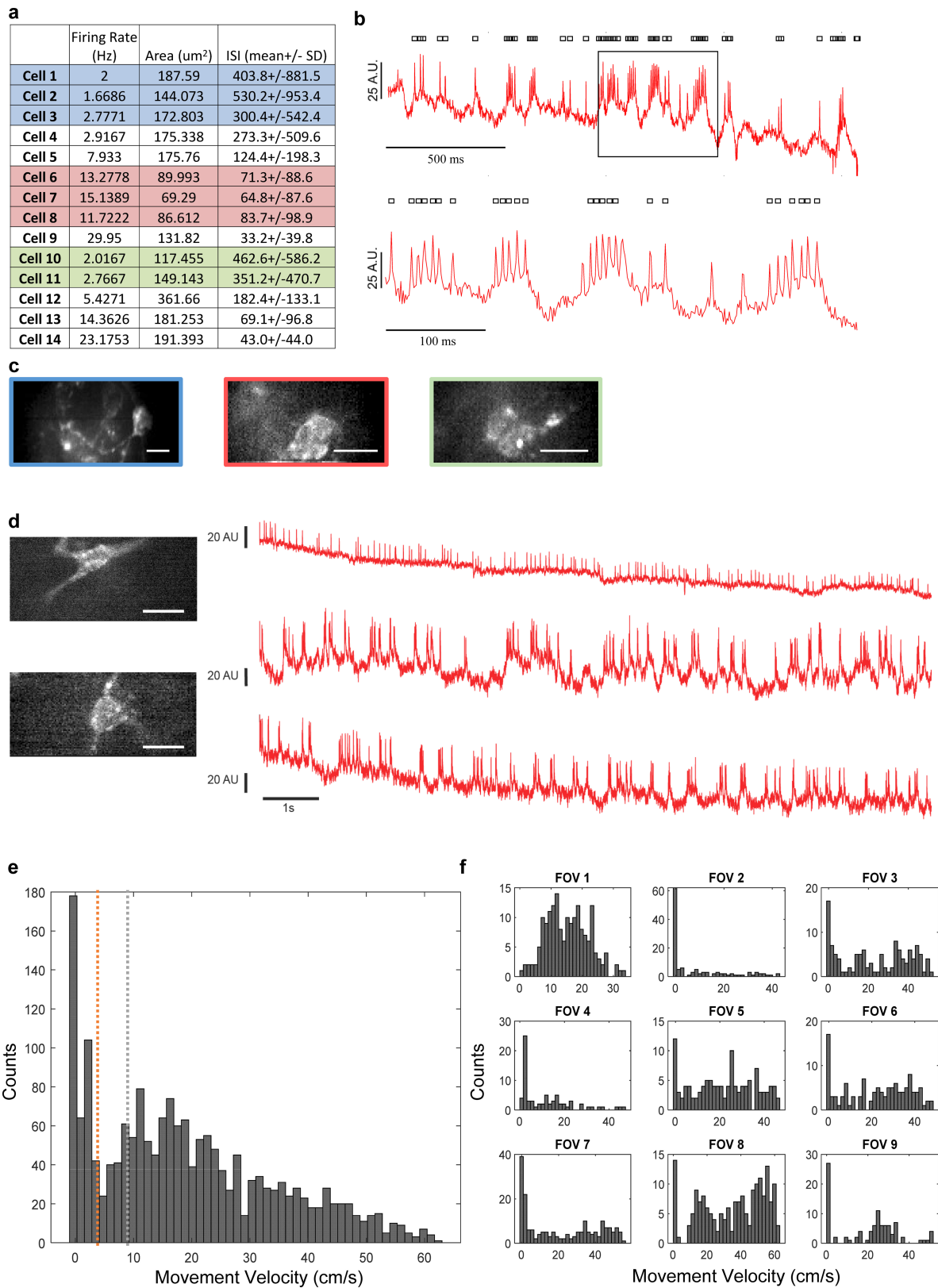
with 4-aminopyridine, and QuasAr3-s (blue), paQuasAr3-s (brown), and SomArchon (red) fluorescence responses during neuronal activity evoked with CoChR-mTagBFP2-K_V2.2$_{motif}$. Acquisition rate, about 500 Hz. Blue light pulses (470/20 nm, 2 ms per pulse, 10 Hz; vertical blue bars) were used to activate CoChR to evoke spiking. **c, d**, Quantification of $\Delta F/F$ (**c**) and SNR (**d**) per action potential across all recordings ($n = 18, 14, 9, 13$, and 14 neurons from 1, 2, 2, 2, and 2 mice for ASAP3-Kv, Voltron-ST/JF$_{525}$, QuasAr3-s, paQuasAr3-s, and SomArchon, respectively). Box plots as in Fig. 1. *$P < 0.01$, Wilcoxon rank-sum test; see Supplementary Table 2 for statistics. **e**, Photobleaching curves of ASAP3-Kv, Voltron-ST/JF$_{525}$, and SomArchon under continuous illumination ($n = 11, 8$, and 17 neurons from 1 culture, respectively).

Extended Data Fig. 6 | SomArchon enables both local dendritic and population imaging of neurons in multiple brain regions in vivo.
a, Fluorescence images of selected FOV in motor cortex (left) with selected ROIs corresponding to somas of 3 neurons (right) ($n = 1$ FOV from 1 mouse). Scale bar, 50 μm. **b**, Representative fluorescence traces from **a** with detected spikes (black ticks). **c**, Fluorescence image of a hippocampal neuron expressing SomArchon with ROIs selected at the soma and on 4 proximal dendrites ($n = 1$ neuron from 1 mouse). Scale bar, 20 μm. **d**, Optical voltage traces from the selected ROIs shown in **c**. **e**, Fluorescence image of a striatal neuron expressing SomArchon with ROIs selected at the soma and on 3 proximal dendrites ($n = 1$ neuron from 1
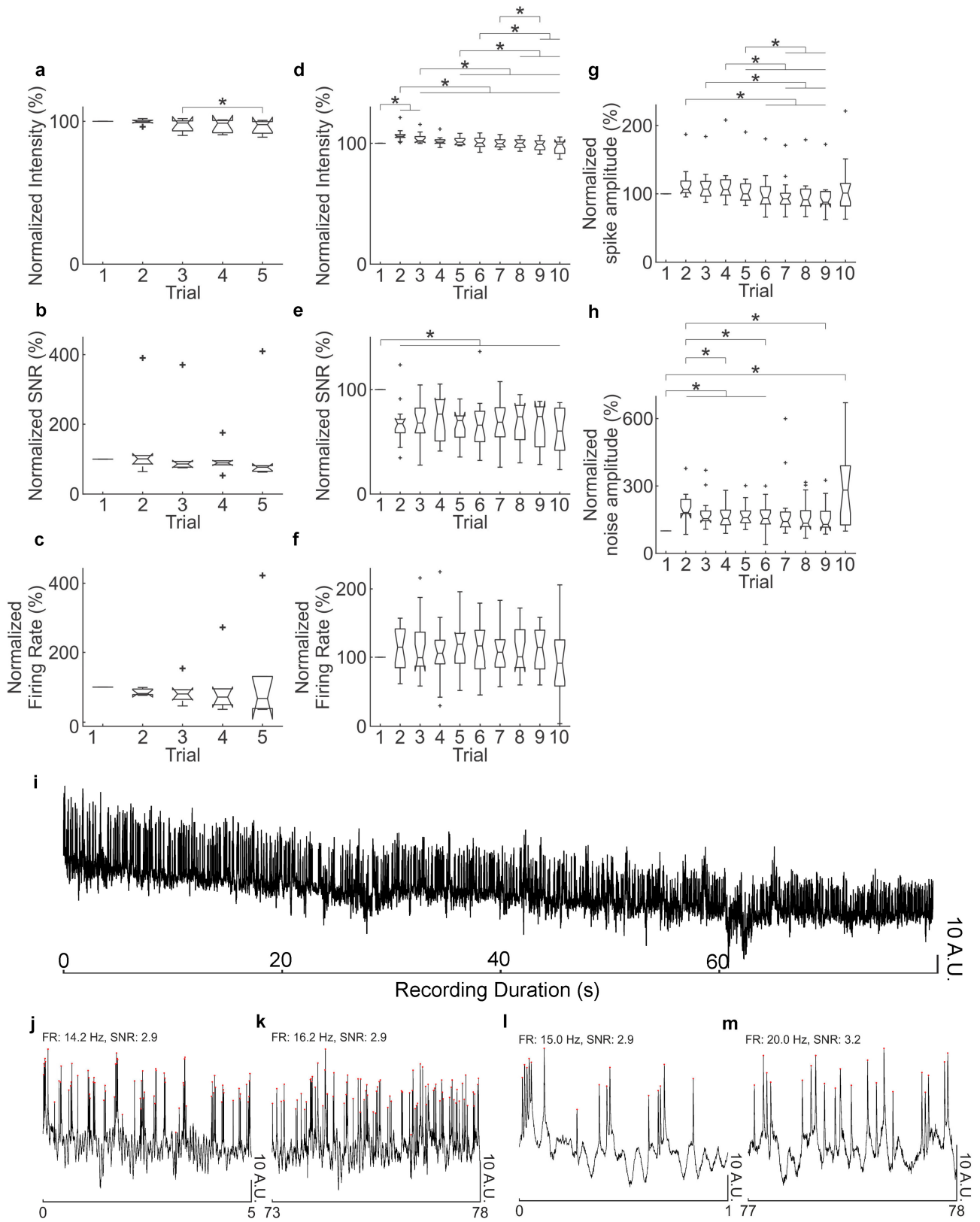
mouse). Scale bar, 20 μm. **f**, Optical voltage traces from the selected ROIs shown in **e**. Black arrows in **d**, **f** highlight instances in which dendritic voltages differed visibly from those on the soma. **g**–**k**, In vivo population voltage imaging in the hippocampus CA1 region ($n = 14$ FOVs from 3 mice). **g**, **i**, Average intensity projection image for each video (top), with identified ROIs (bottom). **h**, **j**, Optical voltage traces for each neuron shown in **g**, **i**, respectively, with colours matching corresponding ROI colours. Panels show 1.2 s of simultaneously recorded voltage for all neurons (left), and a period with prominent spikes (right). Image acquisition rate for all recordings, 826 Hz.

a

	Firing Rate (Hz)	Area (um²)	ISI (mean+/- SD)
Cell 1	2	187.59	403.8+/-881.5
Cell 2	1.6686	144.073	530.2+/-953.4
Cell 3	2.7771	172.803	300.4+/-542.4
Cell 4	2.9167	175.338	273.3+/-509.6
Cell 5	7.933	175.76	124.4+/-198.3
Cell 6	13.2778	89.993	71.3+/-88.6
Cell 7	15.1389	69.29	64.8+/-87.6
Cell 8	11.7222	86.612	83.7+/-98.9
Cell 9	29.95	131.82	33.2+/-39.8
Cell 10	2.0167	117.455	462.6+/-586.2
Cell 11	2.7667	149.143	351.2+/-470.7
Cell 12	5.4271	361.66	182.4+/-133.1
Cell 13	14.3626	181.253	69.1+/-96.8
Cell 14	23.1753	191.393	43.0+/-44.0

b

c

d

e

f

Extended Data Fig. 7 | See next page for caption.

Extended Data Fig. 7 | Properties of striatal neurons and movement thresholds. a, Average firing rate, size, and interspike interval (ISI) for 14 neurons recorded in 9 FOV in 2 mice. Cells simultaneously recorded in the same FOV are colour-coded (blue, red and green). Cells in rows with a white background were recorded individually. **b**, Selected trace from cell 9 exhibiting spike bursting (top), and a zoomed-in view of the boxed region (bottom). A.U., arbitrary unit. Identified spikes are indicated by the marks on top of the trace. **c**, Single frame images for FOVs with multiple neurons, colour-coded as in **a**. Scale bars, 20 μm. **d**, Representative optical traces from two Cre-dependent SomArchon-expressing striatal cholinergic interneurons in a ChAT-Cre mouse (left; scale bar, 20 μm),
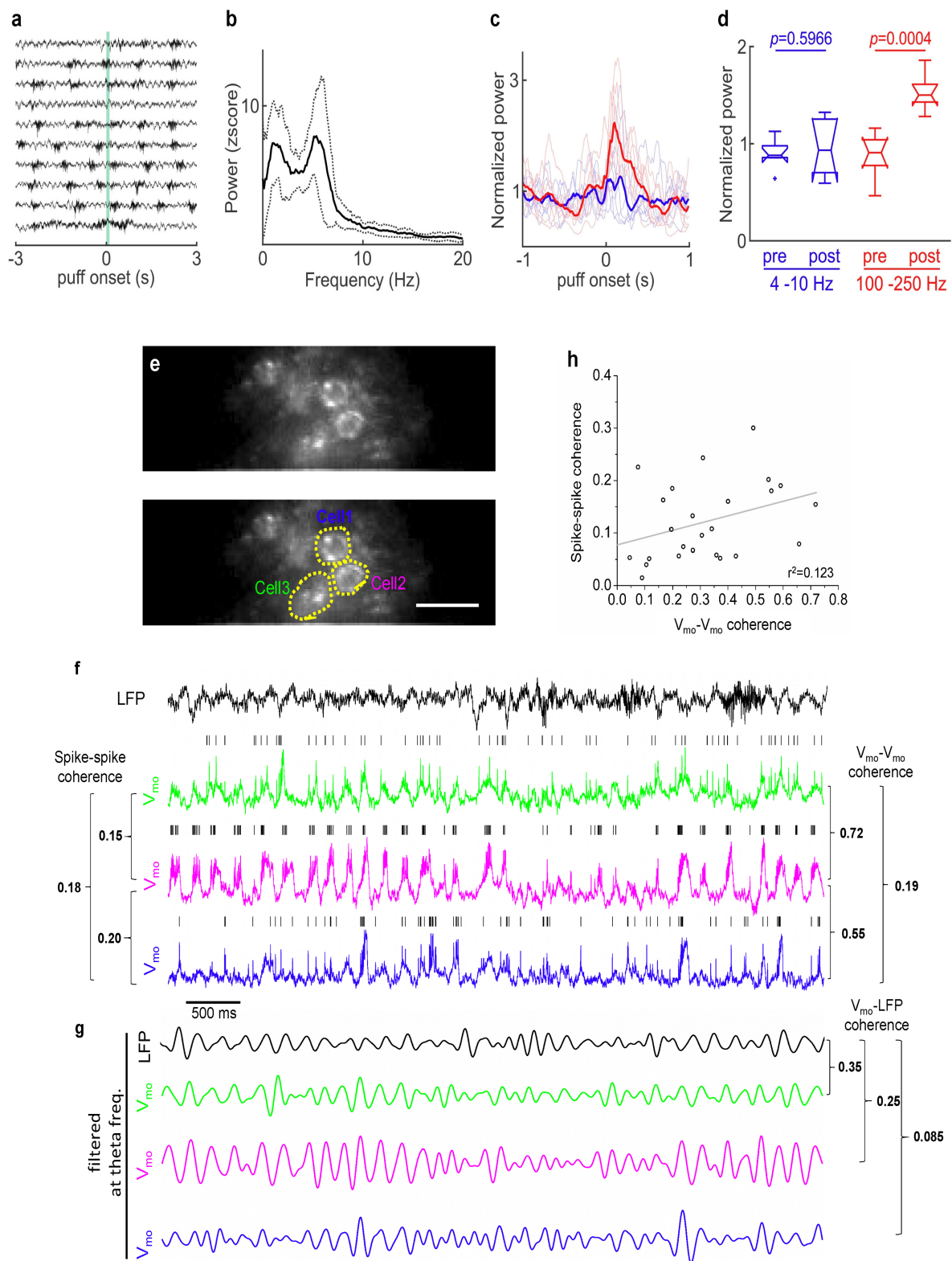
recorded in 3 sessions, while mouse was awake with head fixed and navigating a spherical treadmill (n = 2 neurons from 1 mouse). Top trace corresponds to top neuron on left; two bottom traces correspond to bottom neuron. Image acquisition rate, 826 Hz. **e**, Histogram of instantaneous movement speeds for all FOVs shown in Fig. 3 (nine FOVs in two mice). Instantaneous movement speed was calculated as average speed during each 0.5-s time interval. Red line, threshold for low movement speed identification; green line, threshold for high movement speed identification. **f**, Histogram of instantaneous movement speed for individual FOVs analysed.

Extended Data Fig. 8 | See next page for caption.

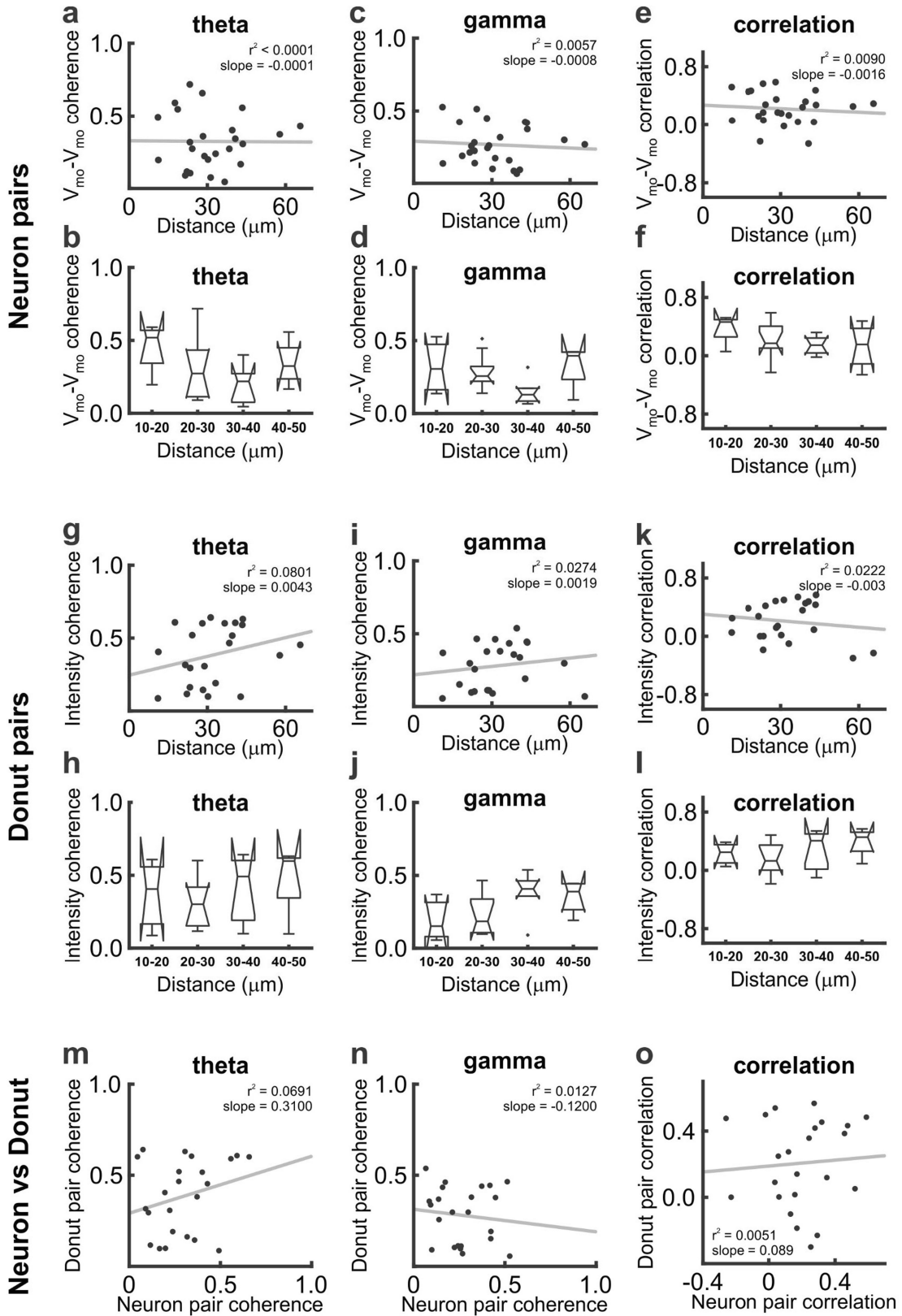**Extended Data Fig. 8 | In vivo SomArchon performance over time in the striatum and hippocampus of awake mice. a–h**, Average fluorescence intensity, SNR per spike, and firing rates of neurons in the striatum and hippocampus of awake mice, over multiple trials. **a–c**, In each striatal recording session, we performed 5 trials, each 12-s long, with inter-trial intervals of 30–60 s. Average fluorescence intensity (**a**) decreased slightly; spike SNR (**b**) and firing rates (**c**) remained constant throughout the recording session (repeated-measures analysis of variance (ANOVA), $n = 6$ neurons in 5 FOVs from 1 mouse). **d–h**, In each hippocampal recording session, we performed 10 trials, each 6-s long, with inter-trial intervals of 20–30 s. Average fluorescence intensity (**d**) showed a slight but significant decrease across trials. SNR (**e**) decreased between the first and second trials but not afterwards, and firing rate (**f**) remained constant. Spike amplitude (**g**) fluctuated randomly over trials, and there was a significant increase in baseline noise (**h**) between the first and second trials (repeated-measures ANOVA; *$P < 0.05$, post-hoc test: Tukey's HSD test, $n = 16$ neurons in 7 FOVs from 4 mice, Supplementary Table 2). Measurements were normalized to the first trial for each neuron. Box plots as in Fig. 4. **i–m**, A representative continuous optical trace of a hippocampal neuron over 80 s in an awake, head-fixed mouse (**i**), with zoomed-in views (**j–m**) at the beginning and end of the recording highlighting comparable firing rates and SNRs ($n = 16$ neurons in 7 FOVs from 4 mice).

Extended Data Fig. 9 | Analysis of LFP and subthreshold membrane voltage oscillation in the hippocampus. a, Example hippocampal LFP recordings from a session with ten trials, aligned to the onset of an air puff (green shading) directed to one eye in awake, head-fixed mice. **b**, LFP power spectrum shows strong theta oscillations. Mean ± s.d., $n = 10$ trials in 1 session. **c**, Oscillation power at high frequencies (100–250 Hz, red) and at theta frequencies (blue), aligned to puff onset. Each thin line represents an individual recording session, and the thick lines denote means ($n = 7$ sessions in 4 mice). **d**, Eye puff evoked a significant increase in LFP power at high frequency, but not at theta frequency (theta frequency $P = 0.5966$; high frequency $P = 0.0004$; two-tailed

paired Student's t-test, $n = 7$ sessions in 4 mice). Box plots as in Fig. 4. **e**, Fluorescence image of a representative FOV (top) with selected ROIs (bottom). **f**, Membrane voltage recorded optically (V_{mo}) from neurons identified in **e**, and simultaneously recorded LFPs. Black vertical ticks above V_{mo}s denote spikes. Spike–spike coherence values between neurons are shown on the left and V_{mo}–V_{mo} theta coherence values are shown on the right. **g**, Theta-frequency-filtered LFPs and V_{mo}s for the four traces shown in **f**. V_{mo}–LFP coherence values are shown on the right. **h**, Scatter plot of V_{mo}–V_{mo} theta frequency coherence and spike–spike coherence from all neuron pairs, fitted with a linear regression ($n = 25$ pairs, $P = 0.08$, t-statistic, $r^2 = 0.12$).

Extended Data Fig. 10 | See next page for caption.

Extended Data Fig. 10 | Pairwise coherence and correlation measures over spatial distance. To investigate the potential of background fluorescence signals under wide-field imaging to produce shared crosstalk signals on neuron pairs, we examined the relationship of various coherence and correlation measures between neurons and background fluorescence over spatial distance. **a, b,** Pairwise coherence at theta frequencies between neurons. V_{mo}–V_{mo} coherence did not decrease significantly with spatial distance. (**a**, $n = 25$ pairs analysed with spatial distance of 11–66 μm, centre to centre; **b**, $n = 23$ pairs within 50 μm of each other; $F = 1.44$, $P = 0.26$, one-way ANOVA). **c, d,** Pairwise V_{mo}–V_{mo} coherence at gamma frequencies (30–50 Hz) was not dependent on spatial distance (**c**, $n = 25$ pairs; **d**, $n = 23$ pairs within 50 μm of each other; $F = 2.10$, $P = 0.13$, one-way ANOVA). **e, f,** Pairwise correlation between neurons did not decrease significantly with spatial distance (**e**, $n = 25$ pairs; **f**, $n = 23$ pairs within 50 μm of each other; $F = 1.00$, $P = 0.42$, one-way ANOVA). **g–l,** Same analysis as in **a–f** performed in background doughnut ROIs surrounding each neuron (Methods). Similar to results from neuron pairs, we found that theta frequency coherence between background doughnut ROIs was not dependent on spatial distance (**g**, $n = 23$ pairs; **h**, $n = 21$ pairs; $F = 0.65$, $P = 0.59$, one-way ANOVA), nor was gamma frequency coherence (**i**, $n = 23$ pairs; **j**, $n = 21$ pairs; $F = 1.93$, $P = 0.16$, one-way ANOVA), or the correlation coefficient (**k**, $n = 23$ pairs; **l**, $n = 21$ pairs; $F = 1.02$, $P = 0.41$, one-way ANOVA). **m–o,** The coherence between neurons and their corresponding doughnuts was not correlated at theta frequency (**m**), at gamma frequency (**n**), or for the Pearson correlation coefficients (**o**). Box plots are as in Fig. 4.

Corresponding author(s): Xue Han, Edward S. Boyden

Last updated by author(s): Apr 25, 2019

Reporting Summary

Nature Research wishes to improve the reproducibility of the work that we publish. This form provides structure for consistency and transparency in reporting. For further information on Nature Research policies, see Authors & Referees and the Editorial Policy Checklist.

Statistics

For all statistical analyses, confirm that the following items are present in the figure legend, table legend, main text, or Methods section.

n/a	Confirmed	
☐	☒	The exact sample size (*n*) for each experimental group/condition, given as a discrete number and unit of measurement
☐	☒	A statement on whether measurements were taken from distinct samples or whether the same sample was measured repeatedly
☐	☒	The statistical test(s) used AND whether they are one- or two-sided *Only common tests should be described solely by name; describe more complex techniques in the Methods section.*
☒	☐	A description of all covariates tested
☐	☒	A description of any assumptions or corrections, such as tests of normality and adjustment for multiple comparisons
☐	☒	A full description of the statistical parameters including central tendency (e.g. means) or other basic estimates (e.g. regression coefficient) AND variation (e.g. standard deviation) or associated estimates of uncertainty (e.g. confidence intervals)
☐	☒	For null hypothesis testing, the test statistic (e.g. *F*, *t*, *r*) with confidence intervals, effect sizes, degrees of freedom and *P* value noted *Give P values as exact values whenever suitable.*
☒	☐	For Bayesian analysis, information on the choice of priors and Markov chain Monte Carlo settings
☒	☐	For hierarchical and complex designs, identification of the appropriate level for tests and full reporting of outcomes
☒	☐	Estimates of effect sizes (e.g. Cohen's *d*, Pearson's *r*), indicating how they were calculated

Our web collection on statistics for biologists contains articles on many of the points above.

Software and code

Policy information about availability of computer code

Data collection	Data were recorded using NIS-Elements Advance Research software v4.60.00, HC Image 4.5, OmniPlex system 1.6.0, and MATLAB 2014b.
Data analysis	Data were analyzed offline using NIS-Elements Advance Research software v4.60.00, OriginPro 8 (OriginLab), C, Excel 2016 (Microsoft), ImageJ(Fiji) 1.52i, Python 3.6.8. and 3.7.1, BoxPlotR, and MATLAB 2017a, 2018a, 2018b.

For manuscripts utilizing custom algorithms or software that are central to the research but not yet described in published literature, software must be made available to editors/reviewers. We strongly encourage code deposition in a community repository (e.g. GitHub). See the Nature Research guidelines for submitting code & software for further information.

Data

Policy information about availability of data

All manuscripts must include a data availability statement. This statement should provide the following information, where applicable:

- Accession codes, unique identifiers, or web links for publicly available datasets
- A list of figures that have associated raw data
- A description of any restrictions on data availability

Code availability. Computer codes used to generate results for this study are available at https://github.com/HanLabBU/somarchon-imaging.
Data availability. The data that support the findings of this study are available from the corresponding author upon reasonable request; raw data essential to the work is avalible online at nature.com. Sequences of the reported proteins are available at Genbank at the following accession codes: SomArchon MN091368; SomArchon-P2A-CoChR-KV2.1motif, MN091369.

Field-specific reporting

Please select the one below that is the best fit for your research. If you are not sure, read the appropriate sections before making your selection.

☒ Life sciences   ☐ Behavioural & social sciences   ☐ Ecological, evolutionary & environmental sciences

For a reference copy of the document with all sections, see nature.com/documents/nr-reporting-summary-flat.pdf

Life sciences study design

All studies must disclose on these points even when the disclosure is negative.

Sample size	No statistical methods were used to estimate sample size for animal studies throughout. We did not perform a power analysis, since our goal was to create a new technology; in the reference (Dell, R. B., Holleran, S. & Ramakrishnan, R. Sample size determination. ILAR. J. 43, 207–213 (2002)), as recommended by the NIH, "In experiments based on the success or failure of a desired goal, the number of animals required is difficult to estimate..." As noted in the aforementioned paper, "The number of animals required is usually estimated by experience instead of by any formal statistical calculation, although the procedures will be terminated [when the goal is achieved]." These numbers reflect our past experience in developing neurotechnologies.
Data exclusions	Voltage imaging datasets with significant motion or where no spikes were detected were excluded from analysis. Significant motion was defined as a shift for more than 20 μm in any direction. In Extended Data Figure 1i,j,k data points that corresponded to overlapping neurites were excluded. Data exclusion criteria were not pre-established.
Replication	All attempts at replication were successful. The detailed experimental protocols are provided to facilitate replication by others.
Randomization	There were no treatment conditions to compare in this study. All recording sessions were randomly performed with different voltage sensors or in different brain regions. On recording days, cultured cells or brain slices expressing specific sensors were known. On in vivo recording days, mouse conditions were known. Voltage trace extraction and subsequent analysis were performed with the investigators unaware of specific mouse conditions. For analysis of movement modulation of striatal neuron spiking, a computer algorithm was used to identify periods with different movement parameters. For analysis of spike-phase relationships, or subthreshold membrane voltage relationships, a computer algorithm was used across all conditions. For histology,- sections were selected and images were taken from slides by a researcher not aware of the conditions or antibody used. Cells were also counted and quantified from these sections by a researcher blinded to the experimental conditions or antibody used.
Blinding	

Reporting for specific materials, systems and methods

We require information from authors about some types of materials, experimental systems and methods used in many studies. Here, indicate whether each material, system or method listed is relevant to your study. If you are not sure if a list item applies to your research, read the appropriate section before selecting a response.

Materials & experimental systems

n/a	Involved in the study
☐	☒ Antibodies
☒	☐ Eukaryotic cell lines
☒	☐ Palaeontology
☐	☒ Animals and other organisms
☒	☐ Human research participants
☒	☐ Clinical data

Methods

n/a	Involved in the study
☒	☐ ChIP-seq
☒	☐ Flow cytometry
☒	☐ MRI-based neuroimaging

Antibodies

Antibodies used	Primary antibodies anti-GFAP (1:250, Clone N206/A8, Neuromab) and anti-IBa1 (1:500, 019-19741, Wako Chemicals) and secondary antibodies Alexa Fluor 568 (1:1000, Goat anti-Mouse IgG (H+L) Cross-Adsorbed Secondary Antibody, A11004, InVitrogen) 633 secondary antibodies (1:1000, Goat anti-Rabbit IgG (H+L) Cross-Adsorbed Secondary Antibody, A21070, InVitrogen)were used in the study.
Validation	For anti-GFAP please see: http://neuromab.ucdavis.edu/datasheet/N206A_8.pdf For anti IBa1, please see: http://www.e-reagent.com/uh/Shs.do?now=1550070200673 Validation methods are references in Methods.

Animals and other organisms

Policy information about studies involving animals; ARRIVE guidelines recommended for reporting animal research

Laboratory animals	Species, strain, sex, and age are reported for each experiment in the Methods
Wild animals	The study did not involve wild animals

| Field-collected samples | This study did not involve samples collected in the field. |
| Ethics oversight | Boston University Institutional Animal Care and Use and Biosafety Committee, Massachusetts Institute of Technology Institutional Animal Care and Use and Biosafety Committee |

Note that full information on the approval of the study protocol must also be provided in the manuscript.